https://dx.doi.org/10.1016/j.engstruct.2018.10.078

Experimental assessment on the cyclic behaviour of concrete-filled steel tubular beam-columns with octagonal sections

Junbo Chen[a], Tak-Ming Chan[a,*], Ray Kai Leung Su[b], José Miguel Castro[c]

[a] Dept. of Civil and Environmental Engineering, The Hong Kong Polytechnic University, Hung Hom, Hong Kong, China
[b] Dept. of Civil Engineering, The University of Hong Kong, Pokfulam Road, Hong Kong, China
[c] Faculty of Engineering, University of Porto, Portugal
*tak-ming.chan@polyu.edu.hk

Abstract: This paper presents an experimental investigation on concrete-filled steel tubular beam-columns with octagonal cross-sections (OCFST) under cyclic lateral loading with or without axial load. A total of nine specimens with different parameters, including the normalized axial load level (n) ranging from 0 to 0.5 and concrete compressive cylinder strength (f_c') varying from 30 MPa to 90 MPa, were tested. The failure modes, ultimate strengths, displacement ductility, effective flexural stiffness and cumulative dissipated energy are presented. The results indicate that OCFST beam-columns exhibit a ductile plastic mode and excellent energy dissipation. With the increase of axial load level, the ductility and the energy dissipation capacity decreases, while the ultimate bending capacity firstly increases then drops. Concrete grades seem to have limited influence on the ultimate strength and energy dissipation capacity. The comparison results of the ultimate bending moments and effective flexural stiffness between predictions using EN 1994-1-1 and AISC 360-16 and test results reveal their applicability to the design of OCFST beam-columns.

Keywords: Concrete-filled steel tube; beam-column; octagonal section; cyclic behaviour.

1. Introduction

Concrete-filled steel tubes (CFSTs) have become increasingly popular in the construction industry due to their excellent load-bearing capacity, high ductility and energy dissipation capacity and comparatively low strength and stiffness deteriorations under cyclic loading in comparison to typical steel hollow tubes [1-2]. Over the past few decades, extensive experimental investigations on square, rectangular and circular CFST members have been carried out to advance the knowledge on the structural behaviour of CFST members, including stub column tests [3-9], bond stress tests [10], pure bending tests [11-13] and beam-column tests [14-19], leading to design provisions such as EN 1994-1-1 [20] and AISC 360-16 [21]. Meanwhile, a number of cyclic tests [1-2, 22-27] have been conducted to investigate the ductility and energy dissipation capacity and to evaluate the use of CFST members in structures in seismic regions.

To date, most of the research carried out on CFST members has focussed on square, rectangular and circular sections. Distinct behaviours have been found for CFST members with different cross-sectional shapes. CFST with elliptical or polygonal sections may also be adopted in composite buildings for functional or architectural purposes [28]. Recently, a number of research studies focusing on the elliptical CFST members have been conducted, including both cross-section stub columns behaviour [29-30] and member beam-columns behaviour [31-32]. Steel tubes with polygonal cross-sections in particular have been commonly used in telecommunication structures [33]. The applications of polygonal cross-sections, such as hexagonal and octagonal cross-sections, in composite structures have also attracted the attention of researchers. Tomii et al. [4] tested a total of 268 CFST stub columns, including 148 circular sections, 60 square sections and 60 octagonal sections. The authors found that circular CFSTs and octagonal CFSTs exhibited excellent ductility, while square CFSTs showed a degradative behaviour in compression. The confinement effects of different cross-sectional shapes, eg. square, circular and octagonal sections, were further studied by Susantha et al. [34]. A method to determine the lateral confining pressure provided by the steel tube to the concrete was proposed. It was found that the confinement given by octagonal sections was moderate between circular and square sections. Recently, more investigations on octagonal or polygonal CFSTs have been conducted. Yu et al. [35] proposed a unified formula to determine the axial load bearing capacity of CFST columns with different sections, including circular and polygonal sections and the design expression was subsequently validated against experimental test results. The effect of cross-sectional shapes on the ultimate axial load was studied by Evirgen et al. [36]. Forty-eight CFST stub columns with four different cross-sections, i.e., circular, square, rectangular and hexagonal were tested. Ding et al. [37-38] further investigated, experimentally and numerically, CFST stub columns with hexagonal and octagonal sections. Empirical equations to predict the ultimate bearing capacity of hexagonal and octagonal CFST stub columns were proposed. Liu et al. [39] proposed a plastic-fibre-hinge model to directly calculate the sectional strength of circular and octagonal CFSTs for the application of high strength concrete in CFST structures. Zhu and Chan [40] investigated the use of high strength concrete with a nominal compressive cylinder strength of 100 MPa in triangular, hexagonal and octagonal CFST stub columns. Zhu and Chan [41] further studied the compressive behaviour of octagonal CFST stub columns and design formulae for the cross-section resistance of octagonal CFSTs under axial compression were proposed. To conclude from the aforementioned literature [4, 33-41], the side wall width of an octagonal section is relatively smaller in comparison with square or rectangular sections under the same cross-section areas. Therefore, the local buckling resistance of an octagonal section is expectedly higher than the rectangular counterpart. Moreover, the confinement effect to the concrete core of octagonal CFSTs is comparable to circular CFSTs and is much higher than that developing in square or rectangular CFSTs. However, most of the existing literature for octagonal CFSTs have focussed on stub columns. Research on the structural behaviour of octagonal CFST members under cyclic loading is extremely scarce. Moreover, the cyclic behaviour of CFST members is of great significance for composite structures located in seismic regions. As illustrated in Fig.1, a cyclic test performed on a cantilever element can be seen as an idealized representation of the behaviour of the bottom column segment between the point of inflection and the ground floor during an earthquake. Therefore, to promote the application of polygonal steel tubes in CFST structures, it is of great use to carry out cyclic tests on CFST with octagonal cross-sections.

The primary objective of this paper, following the research [40-41], is to experimentally investigate the structural behaviour of CFST beam-columns with octagonal cross-sections (OCFSTs) under cyclic loading. A total of nine OCFST beam-columns with different parameters, including the axial load level (n) and the concrete cylinder strength ($f_c^{'}$), were tested under cyclical lateral load with or without constant axial load. The axial load level varies from 0 to 0.5, while the concrete cylinder strength ranges from 30 MPa to 90 MPa. The experimental results with regard to ultimate strengths, displacement ductility, initial flexural stiffness and cumulative dissipated energy are presented and discussed.

2. Experimental investigation

2.1 General

An experimental campaign, consisting of nine OCFST beam-columns was carried out. All specimens were tested with a cyclical lateral load applied at the top of the columns, combined with different levels of axial loads. Two parameters were taken into account in this test programme, namely the concrete cylinder compressive strength and the axial load level. Regarding the axial load, four different levels (0, 0.15, 0.3 and 0.5), defined as the ratio between the applied constant load (N_0) to the cross-section axial capacity (N_u), were adopted. EN 1998-1 [42] limits the design axial load to no more than 30% of the design column resistance for all composite columns in moment-resisting frames. An axial load level of 0.5 was adopted to investigate the deterioration effects in columns subjected to cyclic load combined with a higher level of axial load. In this paper, the cross-section axial capacity, N_u, is estimated by the strength superposition of the contributions of steel and concrete in line with EN 1994-1-1 [20] as expressed by Eq. (1), where A_s and A_c are cross-sectional areas of the steel tube and the concrete core, respectively, f_y and $f_c^{'}$ are the yield strength of the steel tube and the concrete compressive cylinder strength, respectively.

$$N_u = A_s f_y + A_c f_c' \qquad (1)$$

To investigate the effect of concrete strength, three different concrete grades with target cylinder compressive strengths of 30 MPa, 50 MPa, and 90 MPa (denoted by C30, C50 and C90 afterwards) were used to fill the octagonal steel tubes. Using different concrete grades also achieved different values of the steel contribution factor (δ) specified in EN 1994-1-1 and defined according to Eq. (2).

$$\delta = \frac{A_s f_y}{A_s f_y + A_c f_c'} \quad (2)$$

The octagonal steel tubes were fabricated by welding two cold-formed half-sections using a welding robot. The half octagonal section was cold bent from steel plates with a nominal thickness of 3 mm and with a nominal yield strength of 355 MPa using a cold bending machine. Fig. 2 indicates the fabrication process of the octagonal steel tubes. The nominal diameter of the circumcircle (D) and the overall width (h) of the design octagonal section are 130.6 mm, 120 mm, respectively. All the OCFST columns were designed having the same dimensions. The actual dimensions of the cross-section of each specimen were precisely measured and the averaged values of the measured diameter (D), width (h) and thickness (t), as well as the detailed information of the test specimens including material parameters and levels of axial load are summarized in Table 1.

Regarding the cross-section slenderness for octagonal sections, no limit is defined in the European codes for static (EN 1994-1-1) and seismic design (EN 1998-1) nor in the corresponding American codes AISC 360-16 and AISC 341-16 [43]. Thus, the limiting criteria for circular and rectangular cross-sections specified in all aforementioned design provisions were used to assess the slenderness of the octagonal section used in this test programme. The cross-section slenderness of the octagonal sections was assessed based on the steel nominal yield strength and the measured yield strength together with the measured D and h values (Table 2). When assessed against EN 1994-1-1 and AISC 360-16 (static provisions), the cross-section slenderness of the octagonal section only slightly exceeded the EN 1994-1-1 specified limit when the criterion for rectangular sections was used and the measured yield strength was considered. As for the limits in EN 1998-1 (seismic provisions), the octagonal section was classified as highly ductile (DCH) if the cross-section slenderness was evaluated based on the criterion for circular sections. However, when the measured steel properties were considered, the octagonal section does not comply with any of the ductility classes specified in EN 1998-1 based on the criterion for rectangular sections. Regarding the limits in AISC 341-16 (seismic provisions), the evaluation considering the nominal yield strength of the steel led to the classification of the octagonal section as a highly ductile member (λ_{hd}) when the circular sections criterion was used, while in other scenarios, the octagonal section was classified as moderately ductile member (λ_{md}) as listed in Table 2. This may indicate that OCFST beam-columns exhibit a ductile plastic mode and good energy dissipation.

2.2 Material tests

To obtain the steel material properties, three tensile coupons were machined in the longitudinal direction from flat portions of an octagonal steel tube and tested on an Instron 8800 Fatigue Testing System with a capacity of 500 kN. The design of the steel coupons complied with the EN ISO 6892-1 [44] standard, as shown in Fig. 3. The basic material properties including elastic modulus (E_s), yield strength (f_y), ultimate tensile stress (f_u), the yield strain (ε_y), the strain when strain hardening initiates (ε_{st}), the strain corresponding to the yield strength (ε_u) and the elongation at fracture based on the original gauge length (ε_f), obtained from coupon tests are listed in Table 3. Full stress-strain curves up to failure of the three tensile coupon tests are presented in Fig. 4.

The concrete used to fill the steel tubes was mixed and cast in the concrete technology laboratory at the Hong Kong Polytechnic University. The concrete was mixed using ordinary Portland cement, aggregates with a maximum size of 20 mm, sand as fine aggregate, water and superplasticizer (high-range water-reducing admixtures). The concrete mix proportions of the three concrete grades based on saturated surface dry (SSD) condition are listed in Table 3.

In total, forty-four standard concrete cylinders with a diameter of 150 mm and a height of 300mm were cast during the concrete infilling of specimens, which consisted of two groups, namely reference group and control group. The reference group consisted of three cylinders for C30 and C50 concrete and five cylinders for C90 concrete. Cylinders of reference group were cured in a water tank at a constant temperature of around 20°C and were tested at 28-day to provide reference strengths. The reference 28-day cylinder strengths (f_{c0}) of the three concrete grades are listed in Table 4. The control group consisted of three cylinders for each specimen infilled with C30 and C50 concrete and five cylinders for each specimen infilled with C90 concrete. Cylinders of the control group were wrapped with cling film to keep the moisture content and to simulate the curing conditions of the concrete filling the tubes. The control cylinders were stored at ambient temperature besides the specimens to make sure cylinders experienced similar conditions as the specimens experienced. Cylinders of the control group were tested on the test day of each specimen.

Four strain gauges with a gauge length of 90 mm were attached to the surface of the standard cylinders at 90-degree to each other to obtain the stress-strain curves and the elastic modulus of concrete. The concrete cylinders were tested by imposing displacement control at a rate of 0.2 mm/min and the testing procedure complied with EN 12390-3:2009 [45]. The concrete compression test results, i.e. the compressive cylinder strengths and the elastic modulus, are summarized in Table 1, while Fig. 5 shows typical stress-strain curves for each concrete grade.

2.3 Test setup, instrumentation and loading protocol

The specimens were tested under combined constant axial load and cyclic lateral load in a reaction frame at the structural laboratory of The University of Hong Kong. A schematic and experimental view of the test setup is presented in Fig. 6. Referring to Fig. 6(b), a schematic front view, the bottom of the specimen was rigidly connected to a steel support by four M30 8.8 grade high strength bolts, while the steel support was fixed onto the rigid platform using six M24 10.9-grade high strength bolts. The other end of the column was connected to the axial and lateral actuators by a steel connector. A condition that can rotate freely at the top of the columns was achieved, with a free effective testing length, L_f, of 870mm (see Fig. 6(b)), which is defined as the vertical distance from the section just above the stiffeners at the bottom of the column to the centre of the hinge on lateral actuator. The axial load was applied to the specimens by using a 500 kN servo-controlled hydraulic actuator prior to the application of the lateral load. For safety reasons, the axial load was applied through a displacement control procedure. The cyclic lateral load was then applied using another 500 kN servo-controlled hydraulic actuator with a maximum stroke of 300 mm. The cyclic loading stage was performed by controlling the top lateral displacement of the specimen. Keeping the axial load constant during the tests through displacement control was a major challenge faced during the tests. Therefore, a tolerance of +/-5% N_0 was set as acceptable tolerance limits and adjustments were made when the tolerance limits were reached. The upper, lower and the average values of the applied load N_0 are summarised in Table 1. Due to the limitation of the capacity of the actuator, the axial load level for specimen S9 was modified to 0.26 instead of using the initial designed value of 0.3.

The instrumentation of the specimens is presented in Fig. 7. In total, ten linear variable displacement transducers (LVDTs) were installed to measure the corresponding displacements. LVDTs 1-2 (with reference to the frame), LVDTs 3-5 (with reference to the rigid platform), and LVDTs 6-8 (with the reference to the steel support) were placed to measure the relative sliding and uplift between the rigid platform and the reaction frame, the sliding and uplift between the steel support and the rigid platform, and the sliding and uplift between the specimen and the steel support, respectively. LVDT 9 measured the sliding between the specimen and the connector, and LVDT 10 controlled the drift value of target displacement in each cycle. Numbers of strain gauges were mounted to the specimens at sections A-A and B-B, 50 mm and 150 mm away from the section just above the vertical stiffeners, as shown in Fig. 7. At section B-B, only longitudinal strains were measured, while at section A-A, for the tests without axial load (i.e. S1, S4 and S7), only longitudinal strains were measured, and for the tests with axial load (i.e. S2, S3, S5, S6, S8 and S9), both longitudinal and hoop strains were measured.

The lateral cyclic loading protocol was based on the SAC loading protocol [46], as shown in Fig. 8, in which six cycles are imposed for specimen drift ratios at 0.375%, 0.50% and 0.75%, four cycles at 1%, two cycles at 1.5% and 2%, and two cycles for the remaining drift ratio levels with an increment of 1% until failure of the specimen was reached. The drift ratio is defined as the ratio of lateral displacement divided by the column effective length (L_f), as shown in Fig 6(b).

3. Experimental results and discussion

3.1 Failure modes

Generally, significant outward local buckling developed at the base of the columns, which is located just above the vertical stiffeners, as shown in Fig. 9(a). It was observed that the outward bulge was firstly initiated on the compression side after the longitudinal compression strain of the steel tube exceeded the yield strain (ε_y). Subsequently, the bulge formed on the opposite side of the steel tube when the lateral load was reversed. The outward local buckling phenomenon became more obvious with the increase of the lateral displacement. For the specimens with high axial load level, the bulge grew as a complete ring, similar to the elephant foot buckling, as depicted in Fig. 9(b). The three specimens without axial load (S1, S4 and S7) failed by fracture of the steel tube after significant outward local buckling, which may be due to the relatively large drift ratios (around 7.5%) at the end of the test for these specimens. Cracking of the steel tube initiated when the drift ratio reached around 6% and propagated with the increase of the drift until fracture. The bottom region of the failed specimens was cut after testing to observe the failure of the infilled concrete. As shown in Fig. 9(c), the concrete core crushed at the locations where outward local buckling occurred and several horizontal cracks propagated at the concrete crushing region.

3.2 Global lateral behaviour

The global cyclic behaviour of the specimens is examined on the basis of the lateral load (P) *vs* lateral drift (Δ) curves plotted in Fig. 10. It should be noted that all the relative sliding and uplift due to the bolted connections were deducted from the readings of LVDT 10 when calculating the lateral drift (Δ). Due to the pin-pin condition of the actuator, there was a slight tilt of the vertical actuator during the cyclic tests, which had an influence on the axial load and the measured lateral load. The change of the axial load due to the tilt of the actuator is minimal because of the comparatively long distance between the two hinges of the actuators, as illustrated in Fig. 6(b). Therefore, the effect of tilt on the axial load could be ignored. However, the horizontal component introduced by the tilt of the vertical actuator was taken into account in the calculation of the lateral load. Moreover, the influence due to the fact that the free rotation point of the applied load is higher than the point where the lateral load applied was accounted for as well in the calculation.

It can be seen from Fig. 10 that the hysteretic behaviour of the specimens subjected to axial load exhibits lower pinching levels in comparison to the specimens without axial load (S1, S4 and S7). Conversely, more pronounced softening was observed for the specimens subjected to axial load, reflecting the development of P-Delta effects in the specimens. Due to the brittle nature of concrete, severe horizontal cracks propagated in the specimens without axial load as shown in Fig. 9(c). After the propagation of the horizontal cracks, when the applied lateral displacement was reversed, no compressive stress was generated until the separated concrete surfaces contact again on the compression side, leading to the pinching effect observed. The presence of axial load, helping to suppress the propagation of cracks in the concrete, contributes to a reduction of the pinching effect. Table 5 summarises the maximum lateral loads (P_{ue}) recorded for all the specimens. The maximum lateral loads were taken as the average values of the maximum lateral loads in the push and pull directions. The lateral load and drift skeleton curves of all the specimens, which were obtained by connecting the peaking point of the first cycle of each drift level in the hysteretic curves, are shown in Fig. 11. A typical lateral load and drift curve for CFST beam-columns is depicted in Fig. 12, in which K, P_{ue}, Δ_y, Δ_u are the initial stiffness, peak lateral load, yield displacement, and the displacement when the lateral load drops to 85% of P_{ue}, respectively. The initial stiffness K can be determined using a linear regression of lateral load over lateral displacement between 0 kN and a lateral load of 20% P_{ue}. The yield displacement can be calculated as $\Delta_y = P_{ue}/K$ [47]. It should be noted that the initial stiffness is only used to calculate the yield displacement and is not related to the effective flexural stiffness of the composite cross-section (K_{ie}), which will be discussed in Section 3.5.1. The ductility ratio (μ), as defined in Eq. (3), was used to evaluate the ductility of the OCFST members subjected to a constant axial load and cyclic flexural loading [45]. The ductility value for each specimen was taken as the average of the ductility values in the push and pull directions and the calculation results are summarised in Table 5.

$$\mu = \frac{\Delta_u}{\Delta_y} \tag{3}$$

As anticipated, both the maximum lateral load and ductility decreased with the increase of the axial load level, as indicated in Fig. 11. When the axial load level was increased from 0 to 0.5 for specimens infilled with C30 concrete, P_{ue} and μ dramatically decreased by 24% and 49%, respectively, whereas when the axial load level was increased from 0 to 0.3 for specimens infilled with C50 and C90 concretes, P_{ue} decreased by 17% and 22%, and μ decreased by 35% and 26%, respectively. These observations can be justified by the P-Δ effects resulting from the applied load N_0 and also by the axial compression and bending interaction behaviour since the axial force has a direct influence on the ultimate bending capacity of the members.

3.3 Strain analysis

Figs. 13-15 present the lateral load versus strain curves of typical specimens, namely S1 (without axial load), S2 (subjected to a moderate axial load level) and S9 (subjected to a high axial load level). The yield strain (ε_y) of the steel obtained from the material tests is also highlighted in these figures (please refer to Fig. 7 for the numbering system of the strain gauges). It can be seen from these figures that the lateral load and strain relations show a linear range in the initial loading stage. After yielding of the steel, both longitudinal and hoop strains at A-A section (see Figs. 13(b), 14(b-c) and 15(b-c)) increased dramatically and residual strains could be observed upon unloading, indicating that local buckling initiated and developed significantly. It is obvious that the strains at the A-A section (see Figs. 13(b), 14(b-c) and 15(b-c)) grew much faster than the strains at B-B section (see Figs. 13(a), 14(a) and 15(a)) after the steel yielded. Focusing on the strains at the B-B section, it is clear that the strains just reached and moderately exceeded the yield strain, indicating that the plastic hinge length exceeded 150 mm (around 1.2h).

3.4 Local behaviour

The behaviour of the plastic hinge region of the OCFST specimens is now examined by inspecting the moment (M) at the base *vs* the drift ratio (θ) curves plotted in Fig. 16. The moment was calculated by superimposing the first-order moment induced by the lateral load with the second-order moment corresponding to the "P-Δ effect", as expressed by Eq. (4), where N_{ver} is the vertical component of the applied load N_0.

$$M = P \cdot L_f + N_{ver} \cdot \Delta \tag{4}$$

As shown in Fig. 16, all specimens exhibited stable hysteretic behaviour curves. Nevertheless, slight pinching can be observed for the specimens tested without axial load (S1, S4 and S7). This conclusion confirms, once again, the beneficial effect of the axial load in reducing the pinching effects.

The maximum moments (M_{ue}) of all the specimens obtained from the test results, which were taken as the averaged values of the maximum lateral loads in the push and pull directions, are listed in Table 5. It can be concluded that, with the increase of the axial load level, the maximum bending moments firstly increase and then decrease, which is in line with the axial force-bending moment interaction curve specified in EN 1994-1-1. In order to demonstrate the contribution of the second-order moment, the first-order moment due to PL_f, the second-order moment due to $N_{ver}\Delta$ and the corresponding percentages were calculated concerning two cases: (1) the point at which the maximum bending moment M_{ue} was attained and (2) the point at which the maximum lateral displacement was attained with corresponding bending moment M_u'. The results of the calculation of the two cases are listed in Table 6 and Table 7, respectively. It should be noted that specimens

S1, S4 and S7 are not included in Table 6 and Table 7 as no axial load was applied to those specimens. As expected, it can be seen from Table 6 and Table 7 that the contribution of the second-order moment increases with the increase in the axial load and the lateral displacement. Comparing the specimens infilled with different concrete grades under the same axial load level, the results indicate that the increase of the ultimate bending moment due to the increase of concrete strength is limited compared with the increase in the axial compression capacity. For instance, when the axial load level is equal to zero, the axial compression capacity approximately doubles when the concrete grade changes from C30 to C90. However, in the same scenario, the increase in the ultimate bending moment is only around 8%, indicating that the use of high strength concrete does not bring significant advantages in terms of flexural resistance.

3.5 Flexural stiffness and energy dissipation capacity

3.5.1 Effective flexural stiffness

To evaluate the flexural stiffness of the OCFST beam-columns, the effective cross-section flexural stiffness (K_{ie}) was calculated. K_{ie} is defined as the secant stiffness corresponding to the moment of $0.2M_{\mathrm{ue}}$ [25, 47] and can be calculated by Eq. (5).

$$K_{\mathrm{ie}} = \frac{0.2M_{\mathrm{ue}}}{\phi} = \frac{0.2M_{\mathrm{ue}}}{(\varepsilon_{\mathrm{t}} - \varepsilon_{\mathrm{c}})/B} \tag{5}$$

where ϕ is the curvature corresponding to $0.2M_{\mathrm{ue}}$, ε_{t} and ε_{c} are the measured strains of the extreme fibres in tension and compression, and B is the overall width of the octagonal section. The calculation results of K_{ie} of all the specimens are listed in Table 5. It can be seen that a higher axial load level is associated to a higher flexural stiffness K_{ie}, which is mainly due to the fact that a higher axial load level in compression contributes to suppressing the propagation of cracks in the concrete part subject to tension.

3.5.2 Energy dissipation

The cumulative hysteresis dissipated energy (E_{h}) is defined as the energy that the OCFST beam-columns dissipate during the cyclic loops and can be evaluated according to Eq. (6).

$$E_{\mathrm{h}} = \sum_{i=1}^{n} (E_i^t + E_i^c) \tag{6}$$

where i is the number of cycles, n is the total number of cycles, and E_i^t and E_i^c are the energies dissipated in the ith half cycle in tension and the ith half cycle in compression, respectively. Two types of cumulative dissipated energy, the cumulative dissipated energy up to the termination of the test (E_{h}) and up to 4% drift ratio ($E_{\mathrm{h,4\%}}$), were evaluated based on the local hysteretic behaviour (M-θ curves as illustrated in Fig. 16). The cumulative dissipated energy of all the specimens is summarised in Table 5.

Regarding the cumulative dissipated energy up to the termination of the test (E_{h}), it is worth noting that the specimens subjected to lower axial load levels dissipated more energy during the hysteretic loops. This is because the axial load level significantly affects the ductility of the OCFST beam-columns and specimens with lower axial load levels could survive more numbers of cycles, normally resulting in a higher cumulative hysteresis dissipated energy. However, when the cumulative dissipated energy up to 4% drift ratio ($E_{\mathrm{h,4\%}}$) are compared, it is found that the strength of concrete appears to have negligible influence on the cumulative energy dissipation and with the increase of the axial load level, the $E_{\mathrm{h,4\%}}$ firstly increases and then decreases.

3.6 Comparison of cyclic behaviour between CCFST and OCFST beam-columns

The lateral load vs drift curves of two CCFST tests available in the literature [2] were selected to compare with those of the OCFST specimens tested in the current experimental programme. It is worth noting that there are no exact equivalent specimens available in the literature, hence particular attention has been paid to select suitable test specimens with similar steel contribution factors and axial load levels in order to obtain qualitative observations. The test parameters of the selected test specimens, including geometric parameters (diameter of the steel tube D, thickness of the steel tube t and effective length L), material parameters (steel yield strength f_y and concrete compressive cube strength f_{cu}), steel contribution factors (δ) and axial load levels (n) are listed in Table 8. It should be noted that the concrete strength reported in the literature [2] was determined by standard cubes with a side length of 150 mm. Eq. (7) [48] was therefore adopted to convert the cube strength f_{cu} into a standard compressive cylinder strength f_c'.

$$f_c' = f_{cu}\left[0.76 + 0.2\log_{10}\left(\frac{f_{cu}}{19.6}\right)\right] \tag{7}$$

As can be seen from Fig. 17(a)-(b), the CCFST specimen SC1-1 exhibits slighter pinching effect compared with specimen S1 tested in this study. With regard to the lateral strength, the circular specimen SC1-1 develops a stable hysteretic behaviour while the octagonal specimen (S1) exhibits strength degradation for drifts levels higher than 40 mm (4.6% drift ratio). It is noted that the steel contribution factor of specimen SC1-1 is higher than that of specimen S1 and the cross-section of the circular steel tube is relatively compact with a cross-section slenderness value $D/(t\varepsilon^2) = 40.9$ (limiting value in EN 1994-1-1 [20] is 90), where D is the outer diameter of steel tube, t is the thickness of steel tube, ε is cross-section slenderness parameter specified in EN 1994-1-1 [20] as $\varepsilon = \sqrt{235/f_y}$, f_y is steel yield strength. The comparison between specimen S3 and specimen SC2-4 shown in Figs. 17(c)-(d) indicates similar hysteretic patterns. The different slopes of the softening branch of the behaviour are a result of the different axial load levels. The circular CFST specimen SC2-4 has a higher axial load level, leading to a more pronounced softening due to a larger contribution of P-Δ effects.

From the above comparisons, it can be concluded that CFST beam-columns with the octagonal section under cyclic flexural loading perform similarly to equivalent circular CFST beam-column counterparts. Therefore, OCFST columns can be favourably used in structures located in seismic regions.

4. Comparisons with design codes

4.1 Cross-sectional resistance

According to EN 1994-1-1, the cross-sectional resistance of CFST beam-columns can be obtained based on the axial force-bending moment interaction curve, as shown in Fig. 18. As specified by EN 1994-1-1 [20, 28], the bending moment capacity can be calculated using the plastic stress distribution method assuming that the steel reaches its yield strength in both compression and tension and the concrete in compression reaches a stress of $\beta f_c'$, where f_c' is the concrete compressive cylinder strength and β is a shape factor for the concrete stress block. Generally, the shape factor is taken as 0.85 for reinforced concrete and composite members. However, according to the European code, for CFST members, this factor should be taken equal to unity. As illustrated in Fig. 18, the nonlinear interaction curve, referring to the dashed line in Fig. 18, can be calculated by varying the position of the neutral axis and establishing equilibrium of forces at the cross-section level. EN 1994-1-1 also allows for a simplified interaction curve using a polygonal diagram (see the solid line in Fig. 18), which can be calculated using four points, referring to points A, B, C and D in Fig. 18. Using the interaction curve, the ultimate bending resistance can be easily determined given a value of compressive axial load N.

AISC 360-16 adopts different stress or strain distribution methods for the evaluation of the cross-section resistance for different cross-section classes, i.e. plastic stress distribution method for compact sections and strain compatibility method, elastic stress distribution method or effective stress-strain method for noncompact or slender sections. Based on the assessment of the cross-section class of octagonal section using both circular and square/rectangular criteria, the octagonal section is classified as compact (see Table

2). Therefore, the plastic stress distribution method was adopted as well to evaluate the bending capacity of the OCFSTs considered in this paper. AISC 360-16 applies different values of the shape factor for circular and square/rectangular CFST beam-columns, i.e. 0.95 for circular sections and 0.85 for square/rectangular sections. As the American code does not prescribe any value for octagonal sections, in this paper, a shape factor of 0.95 was assumed to evaluate the bending capacity according to AISC 360-16.

The ultimate bending moments of the OCFST beam-columns obtained from the test results were compared with those predicted from EN 1994-1-1 and AISC 360-16 to examine the accuracy of the two codes in predicting the flexural strength of OCFST beam-columns. It should be stated that high strength concrete (C90) is not covered both in EN 1994-1-1 and AISC 360-16. However, in this study, the equations specified in these codes were still used to examine their accuracy for high strength concrete. Furthermore, to allow for a direct comparison, all partial safety factors were set to unity. The comparison results are listed in Table 5, indicating that EN 1994-1-1 predicts the ultimate bending moments quite well with an overall mean value of M_{ue}/M_{uc} equal to 1.091 with the corresponding COV of 0.068, where M_{ue} is the ultimate moments obtained from test results and M_{uc} is the ultimate moments predicted based on plastic stress block method. Since the shape factor (β) used in AISC 360-16 was 0.95, which is relatively smaller than unity which was used in EN 1994-1-1, the comparison result is slightly conservative with an overall mean value of M_{ue}/M_{uc} equal to 1.106 with the corresponding COV of 0.064. The applicability of EN 1994-1-1 and AISC 360-16 to the design of OCFST beam-columns seems to be valid and on the conservative side with underestimations of 9.1% and 10.6% of the flexural capacity, respectively. Comparing the specimens infilled with different concrete grades, the predictions using both design codes seem to be more conservative for normal strength concrete than for high strength concrete, as the mean values of M_{ue}/M_{uc} for the specimens infilled with C30, C50 and C90 concrete are 1.148, 1.084 and 1.041 using EN 1994-1-1, respectively, and 1.157, 1.098 and 1.063 using AISC 360-16.

4.2 Effective flexural stiffness

The effective flexural stiffness (K_i) of a composite section can be computed according to Eq. (8), where E and E_c are elastic moduli of the steel and concrete, respectively, I_s and I_c are moment of inertia of the steel tube and concrete, respectively, α is a correction factor to reduce the gross stiffness of the concrete which takes into account of the cracks in the concrete [18].The factor α takes different forms in different codes of practice, e.g. a constant of 0.6 in EN 1994-1-1 and a non-constant (see Eq. (9)) in AISC 360-16, where A_s and A_g are areas of steel tube and composite section.

$$K_i = EI_s + \alpha E_c I_c \tag{8}$$

$$\alpha = 0.45 + 3A_s/A_g \le 0.9 \tag{9}$$

The effective flexural stiffness (K_i) of the OCFST beam-columns obtained from the test results were compared with those predicted from EN 1994-1-1 and AISC 360-16 to examine their accuracy in predicting the flexural stiffness of OCFST beam-columns. The comparisons of the effective flexural stiffness are summarized in Table 5, where K_{ie} is the flexural stiffness obtained from the test results and K_{ic} is the flexural stiffness predicted based on design codes. The results show that EN 1994-1-1 underestimates the effective flexural stiffness by nearly 10% with a mean value of K_{ie}/K_{ic} equal to 1.106 with the corresponding COV of 0.295, and AISC 360-16 predicted the effective flexural stiffness well with a mean value of K_{ie}/K_{ic} equal to 1.034 with the corresponding COV of 0.291, respectively. It is also observed that the flexural stiffness of the OCFST beam-columns increases with the increase of the axial load level, indicating that the axial load level may need to be accounted for in the determination of the flexural stiffness, which is in line with the findings in [18].

5. Conclusions

An experimental investigation on nine CFST beam-columns with octagonal sections under cyclical lateral load with or without axial load was presented in this paper. Three concrete grades with compressive cylinder strengths around 30 MPa, 50 MPa and 90 MPa were used to infill the octagonal steel tubes, while the axial load level ranged from 0 to 0.5. The following conclusions based on the experimental test results can be drawn:

(1) OCFST beam-columns exhibit excellent energy dissipation behaviour. A slight pinching effect was observed from the hysteretic curves when no axial load was applied to the specimens. Pinching effects significantly reduced with the increase of the axial load level.

(2) The ductility of an OCFST member decreases as the axial load level increases. The ultimate bending capacity and the cumulative dissipated energy, evaluated up to a drift ratio of 4%, increases up to a normalised axial load level of 0.3 and then observe a decrease for higher levels of axial load. Increasing the concrete strength has negligible effects on the ultimate bending moment and energy dissipation capacities.

(3) It is viable to extend the current design rules prescribed in EN 1994-1-1 and AISC 360-16 to the design of OCFST beam-columns with slight underestimations of the capacity. However, for conservativeness, a reduction factor may need to be incorporated for the design of OCFST members made with high strength concrete.

(4) EN 1994-1-1 and AISC 360-16 predict the effective flexural stiffness of OCFST beam-columns quite well with an overall mean value of 1.106 and 1.034. The axial load level has an influence on the effective flexural stiffness and it should be taken account in the determination of the effective flexural stiffness.

Acknowledgements

The authors are grateful for the support by the research funding from the Construction Industry Council under the project "Application of Polygonal High Strength Concrete-filled Composite Column in Seismic-resistant Buildings in Hong Kong", for the financial support from The Hong Kong Polytechnic University (PolyU: 1-ZE50/G-YBHV) and for the support from the Chinese National Engineering Research Centre for Steel Construction (Hong Kong Branch). Authors are thankful to the technical staff, Mr C.K. Wong and C.F. Leung of the Civil Engineering Laboratory and Miss L.C. Lo from The University of Hong Kong for their help on the conduction of the experimental works. The authors would also like to thank WoLee steel Co. Ltd. for fabricating the test specimens.

References

[1] Han LH, Yang YF, Tao Z. Concrete-filled thin-walled steel SHS and RHS beam-columns subjected to cyclic loading. Thin-Walled Struct 2003; 41(9): 801-833.
[2] Han LH, Yang YF. Cyclic performance of concrete-filled steel CHS columns under flexural loading. J Construct Steel Res 2005; 61(4): 423-452.
[3] Gardner NJ, Jacobson ER. Structural behavior of concrete filled steel tubes. ACI J Proc. 1967; 64(7): 404-413.
[4] Tomii M, Yoshimura K, Morishita Y. Experimental studies on concrete-filled steel tubular stub columns under concentric loading. In Stability of Structures Under Static and Dynamic Loads, Washington, DC, USA. SSRC/American Society of Civil Engineers (ASCE), Washington, DC, USA, 1977; 718–741.
[5] Schneider SP. Axially loaded concrete-filled steel tubes. J Struct Eng 1998; 124(10): 1125-1138.
[6] Giakoumelis G, Lam D. Axial capacity of circular concrete-filled tube columns. J Construct Steel Res 2004; 60(7): 1049-1068.
[7] Gupta PK, Sarda SM, Kumar MS. Experimental and computational study of concrete filled steel tubular columns under axial loads. J Construct Steel Res 2007; 63(2): 182-193.
[8] Abed F, AlHamaydeh M, Abdalla S. Experimental and numerical investigations of the compressive behavior of concrete filled steel tubes (CFSTs). J Construct Steel Res 2013; 80: 429-439.
[9] Xiong MX, Xiong DX, Liew JR. Axial performance of short concrete filled steel tubes with high- and ultra-high-strength materials. Eng Struct 2017; 136: 494-510.

[10] Roeder CW, Cameron B, Brown CB. Composite action in concrete filled tubes. J Struct Eng 1999; 125(5): 477-484.

[11] Han LH. Flexural behaviour of concrete-filled steel tubes. J Construct Steel Res 2004; 60(2): 313-337.

[12] Probst AD, Kang HK T, Ramseyer C, Kim U. Composite flexural behavior of full-scale concrete-filled tubes without axial loads. J Struct Eng 2010; 136(11): 1401-1412.

[13] Xiong MX, Xiong DX, Liew JR. Flexural performance of concrete filled tubes with high tensile steel and ultra-high strength concrete. J Construct Steel Res 2017; 132: 191-202.

[14] Du YS, Chen Z, Liew JR, Xiong MX. Rectangular concrete-filled steel tubular beam-columns using high-strength steel: Experiments and design. J Construct Steel Res 2017; 131: 1-18.

[15] Du YS, Chen Z, Wang YB, Liew JR. Ultimate resistance behavior of rectangular concrete-filled tubular beam-columns made of high-strength steel. J Construct Steel Res 2017; 133: 418-433.

[16] Prion HG, Boehme J. Beam-column behaviour of steel tubes filled with high strength concrete. Can J Civil Eng 1994; 21(2): 207-218.

[17] Moon J, Lehman DE, Roeder CW, et al. Strength of circular concrete-filled tubes with and without internal reinforcement under combined loading. J Struct Eng 2012; 139(12): 04013012.

[18] Roeder CW, Lehman DE, Bishop E. Strength and stiffness of circular concrete-filled tubes. J Struct Eng 2010; 136(12): 1545-1553.

[19] Silva A, Jiang Y, Castro J.M., Silvestre N, Monteiro R. Experimental assessment of the flexural behaviour of circular rubberized concrete-filled steel tubes. J Construct Steel Res 2016; 122, 557-570.

[20] EN 1994-1-1:2004. Design of composite steel and concrete structures. Part 1–1: general rules and rules for buildings. CEN (European Committee for Standardization); 2004.

[21] ANSI/AISC 360-16. Specification for structural steel buildings. Chicago: American Institute of Steel Construction (AISC); 2016.

[22] Elchalakani M, Zhao XL, Grzebieta R. Concrete-filled steel circular tubes subjected to constant amplitude cyclic pure bending. Eng Struct 2004; 26(14): 2125-2135.

[23] Elchalakani M, Zhao XL. Concrete-filled cold-formed circular steel tubes subjected to variable amplitude cyclic pure bending. Eng Struct 2008; 30(2): 287-299.

[24] Skalomenos KA, Hayashi K, Nishi R, Inamasu H, Nakashima M. Experimental behavior of concrete-filled steel tube columns using ultra-high-strength steel. J Struct Eng 2016; 142(9), 04016057.

[25] Varma AH, Ricles JM, Sause R, Lu LW. Seismic behavior and modeling of high-strength composite concrete-filled steel tube (CFT) beam–columns. J Construct Steel Res 2002; 58(5): 725-758.

[26] Sheehan T, Chan TM. Cyclic response of hollow and concrete-filled circular hollow section braces. P I CIVIL ENG-STR, 2014; 167(SB3), 140-152.

[27] Silva A, Jiang Y, Macedo L, Castro J.M., Monteiro R, Silvestre, N. Seismic performance of composite moment-resisting frames achieved with sustainable CFST members. Front. struct. Civ. Eng. 2016; 10, 312-332.

[28] Liew JR, Xiong MX. Design guide for concrete filled tubular members with high strength materials to Eurocode 4. Research Publishing, 2015.

[29] Chan TM, Huai YM, Wang W. Experimental investigation on lightweight concrete-filled cold-formed elliptical hollow section stub columns. J Construct Steel Res 2015: 115, 434-444.

[30] Liu F, Wang Y, Chan, TM. Behaviour of concrete-filled cold-formed elliptical hollow sections with varying aspect ratios. Thin-Walled Struct, 2017; 110, 47-61.

[31] Sheehan T, Dai XH, Chan TM, Lam D. Structural response of concrete-filled elliptical steel hollow sections under eccentric compression. Eng Struct 2012; 45, 314–323.

[32] Yang H, Liu F, Chan TM, Wang W. Behaviours of concrete-filled cold-formed elliptical hollow section beam-columns with varying aspect ratios. Thin-Walled Struct 2017; 120, 9-28.

[33] Slocum RM. Considerations in the design and fabrication of tubular steel transmission structures. Proceedings of the Fifteenth International Symposium on Tubular Structures - ISTS 15, 27–29 May 2015, Rio de Janeiro, Brazil.

[34] Susantha KAS, Ge HB, Usami T. Uniaxial stress-strain relationship of concrete confined by various shaped steel tubes. Eng Struct 2001; 23(10): 1331-1347.

[35] Yu M, Zha X, Ye J, Li Y. A unified formulation for circle and polygon concrete-filled steel tube columns under axial compression. Eng Struct 2013; 49: 1-10.

[36] Evirgen B, Tuncan A, Taskin K. Structural behavior of concrete filled steel tubular sections (CFT/CFSt) under axial compression. Thin-Walled Struct 2014; 80: 46-56.

[37] Ding FX, Li Z, Cheng S, Yu Z. Composite action of hexagonal concrete-filled steel tubular stub columns under axial loading. Thin-Walled Struct 2016; 107: 502-513.

[38] Ding FX, Li Z, Cheng S, Yu Z. Composite action of octagonal concrete-filled steel tubular stub columns under axial loading. Thin-Walled Struct 2016; 107: 453-461.

[39] Liu SW, Chan TM, Chan SL, So DKL. Direct analysis of high strength concrete-filled tubular columns with circular & octagonal sections. J Construct Steel Res 2017; 129, 301-314.

[40] Zhu JY, Chan TM. Behaviour of polygonal-shaped steel-tube columns filled with high-strength concrete. P. I. Civil Eng-Str & B 2017; 1-17.

[41] Zhu JY, Chan TM. Experimental investigation on octagonal concrete filled steel stub columns under uniaxial compression. J Construct Steel Res 2018; 147, 457-467.

[42] EN 1998-1:2004. Design of structures for earthquake resistance. Part 1: general rules, seismic actions and rules for buildings. CEN (European Committee for Standardization); 2004.

[43] ANSI/AISC 341-16. Seismic provisions for structural steel buildings. Chicago: American Institute of Steel Construction (AISC); 2016.

[44] EN ISO 6892-1:2016. Metallic materials — Tensile testing. Part 1: Method of test at room temperature. CEN (European Committee for Standardization); 2016.

[45] EN 12390-3:2009. Testing hardened concrete. Part 3: Compressive strength of test specimens. CEN (European Committee for Standardization); 2009.

[46] SAC. Protocol for Fabrication, Inspection, Testing, and Documentation of Beam-column Connection Tests and Other Experimental Specimens. Rep. No. SAC/BD-97, 1997.

[47] Liao FY, Han LH, Tao Z, Rasmussen KJ. Experimental behavior of concrete-filled stainless steel tubular columns under cyclic lateral loading. J Struct Eng 2016; 143(4), 04016219.

[48] Mirza S.A., Lacroix E.A. Comparative strength analyses of concrete-encased steel composite columns. J. Struct. Eng. ASCE 2004; 130(12), 1941-1953.

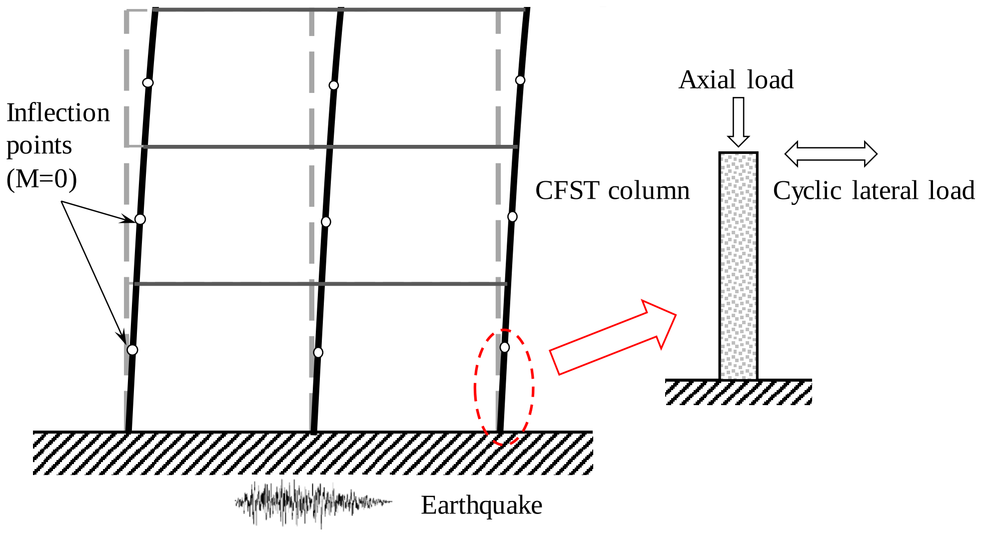

Fig. 1. CFST model in real structure.

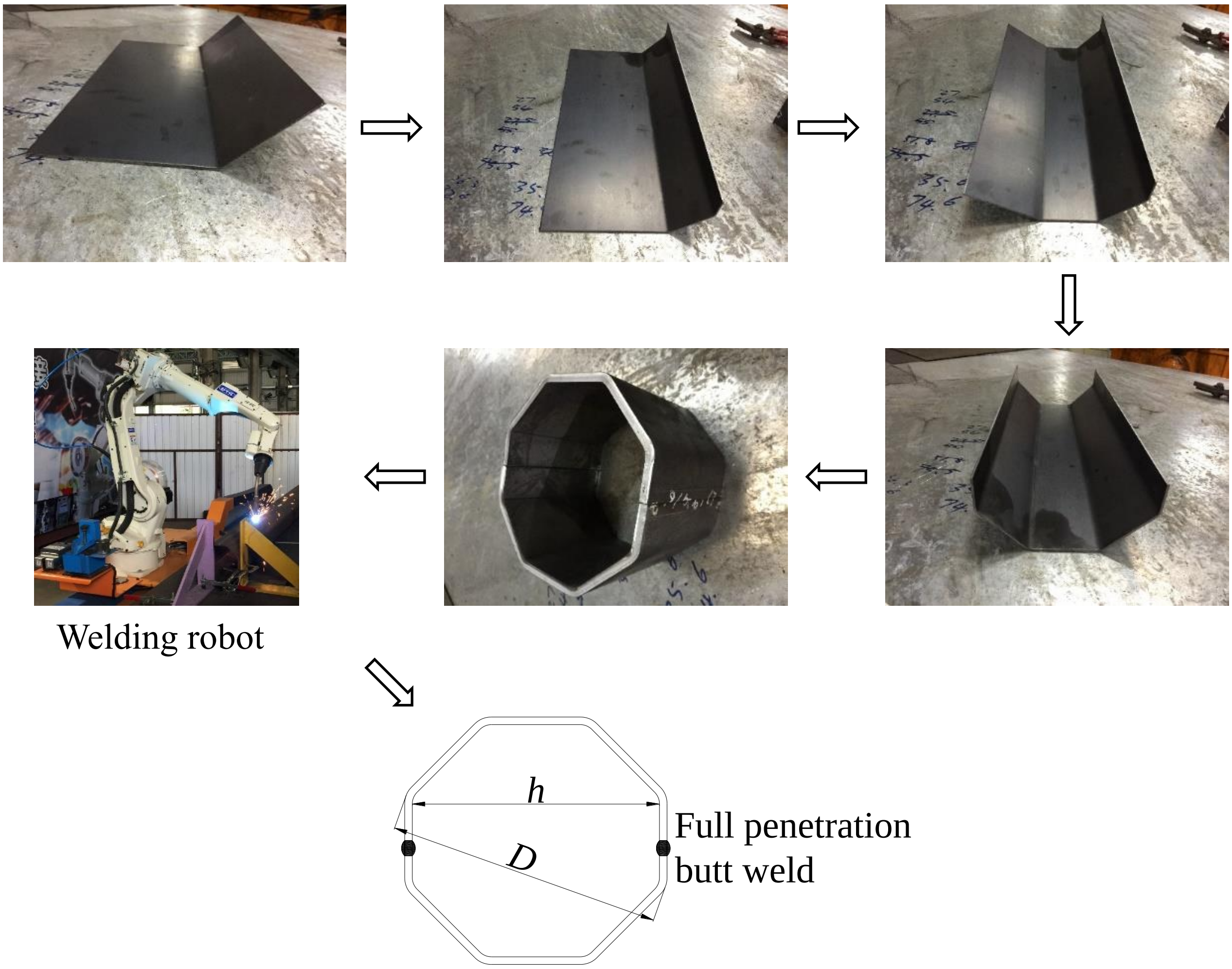

Fig. 2. Fabrication of the octagonal steel tube.

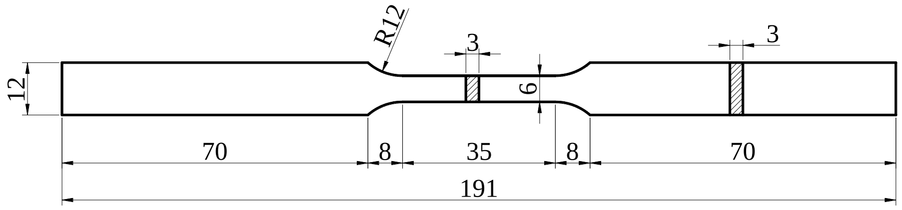

Fig. 3. Dimensions of tensile coupon (Unit: mm).

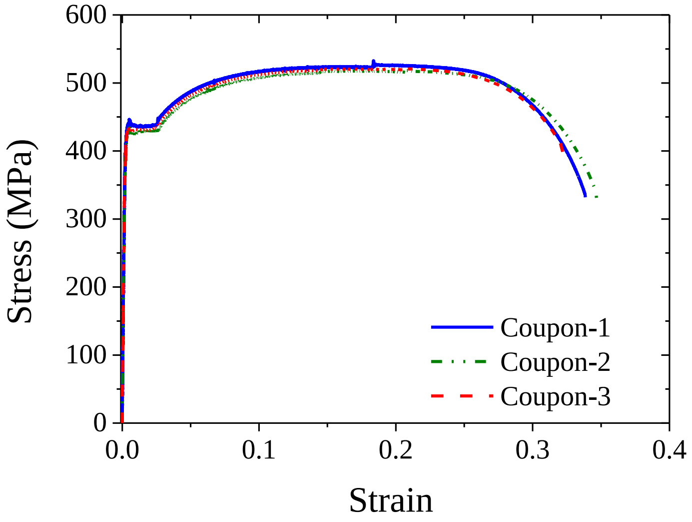

Fig. 4. Stress-strain curves of coupon tests.

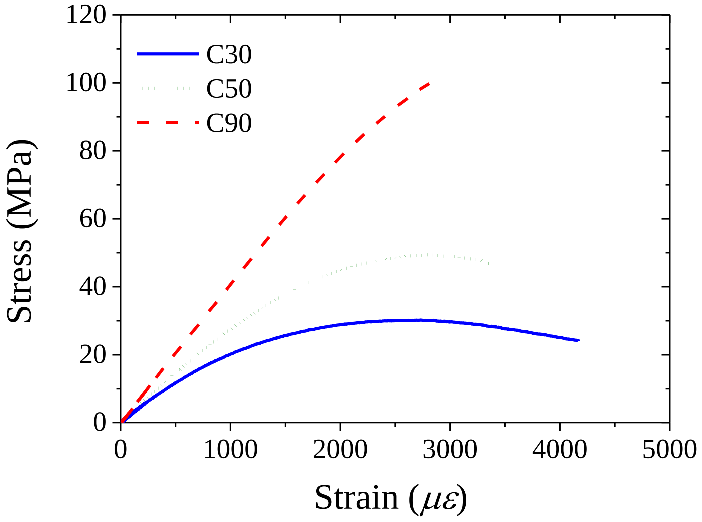

Fig. 5. Stress-strain curves of different concrete grades.

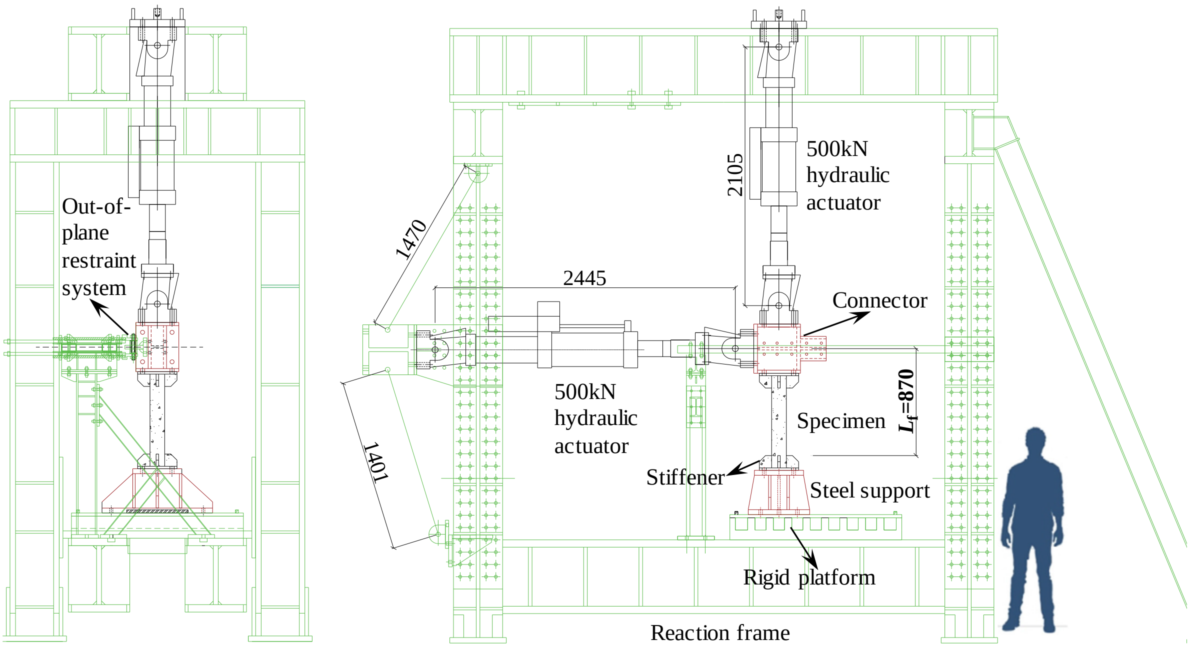

(a) Schematic side view

(b) Schematic front view

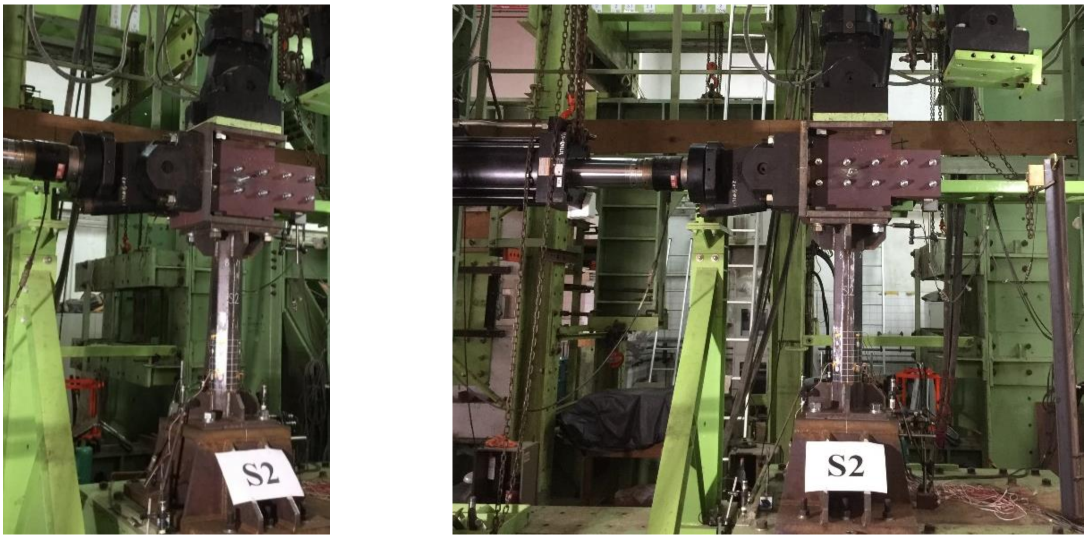

(c) Lateral view of the experiment

(d) Front view of the experiment

Fig. 6. Schematic and experimental views of the test setup (Unit: mm).

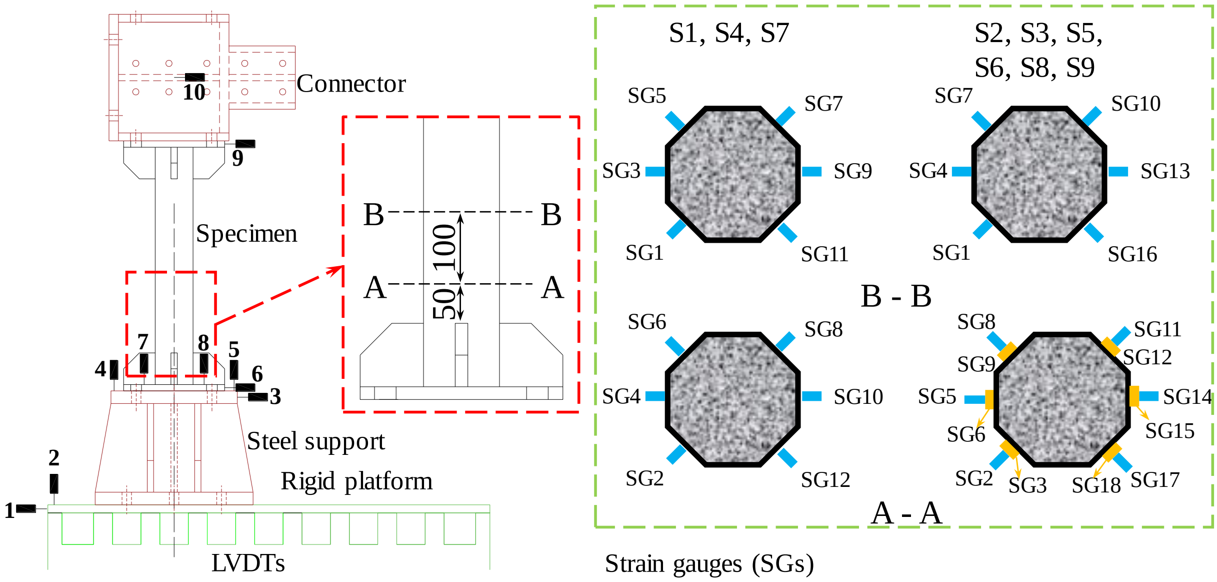

Fig. 7. Instrumentation of the specimens.

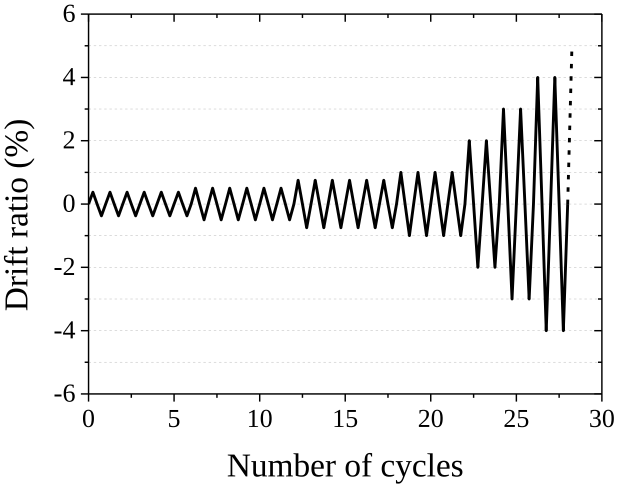

Fig. 8. Lateral loading protocol.

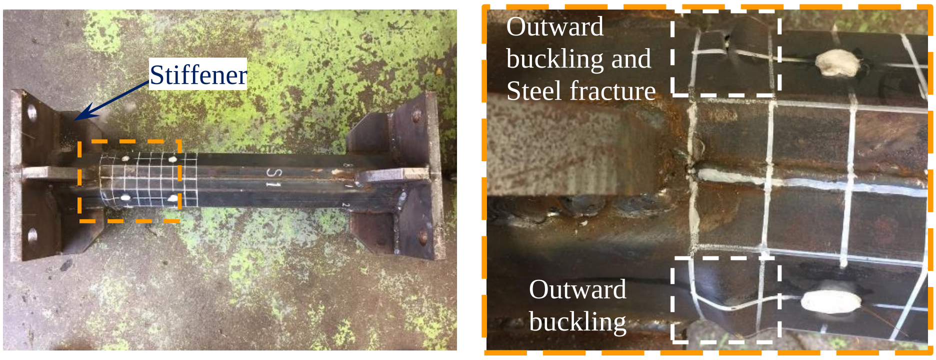

(a) Outward local buckling of the steel tube (specimen S1)

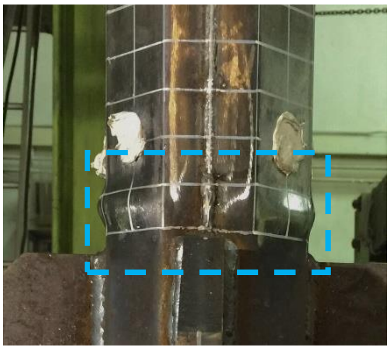

(b) Outward local buckling as elephant foot (specimen S5)

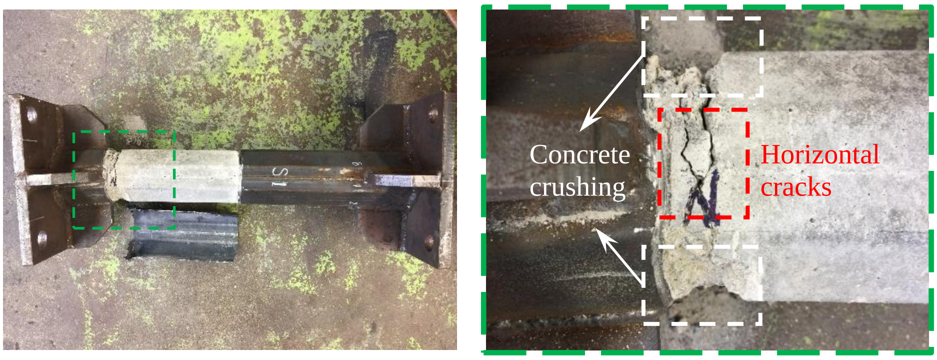

(c) Concrete cracks and concrete crushing (specimen S1)

Fig. 9. Typical failure modes observed during the tests.

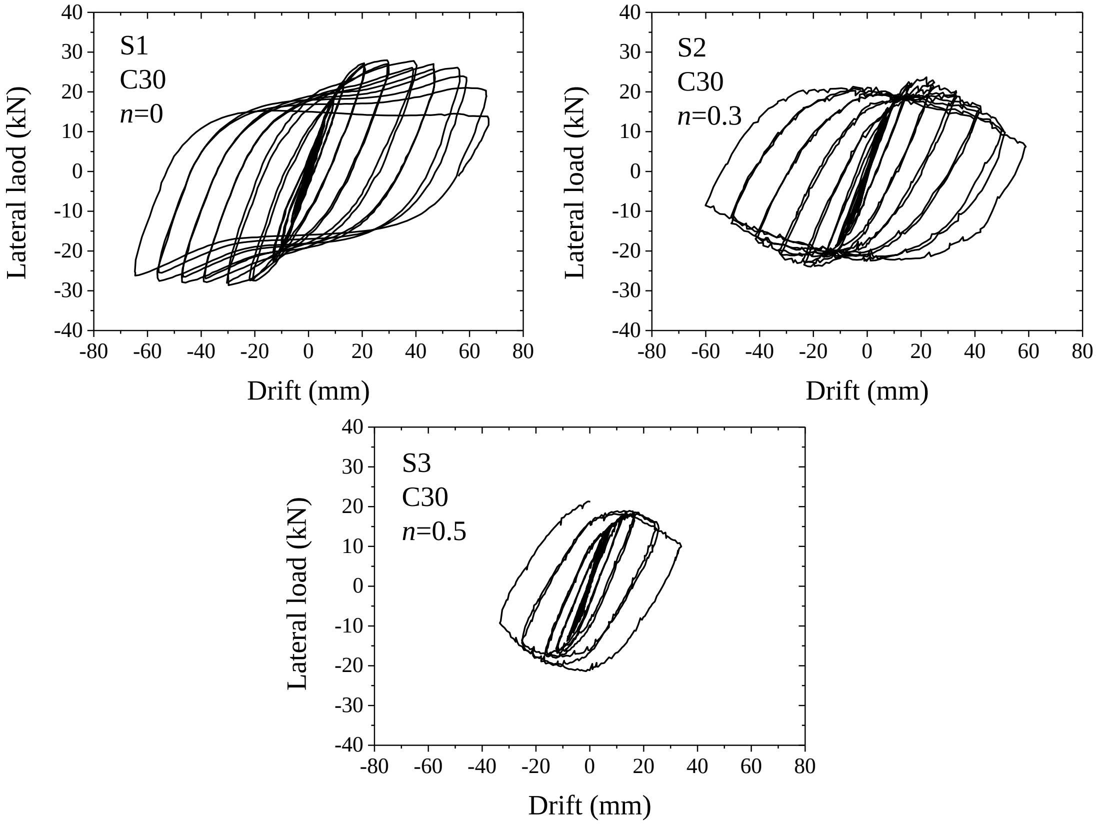

(a) Specimens filled with C30 concrete

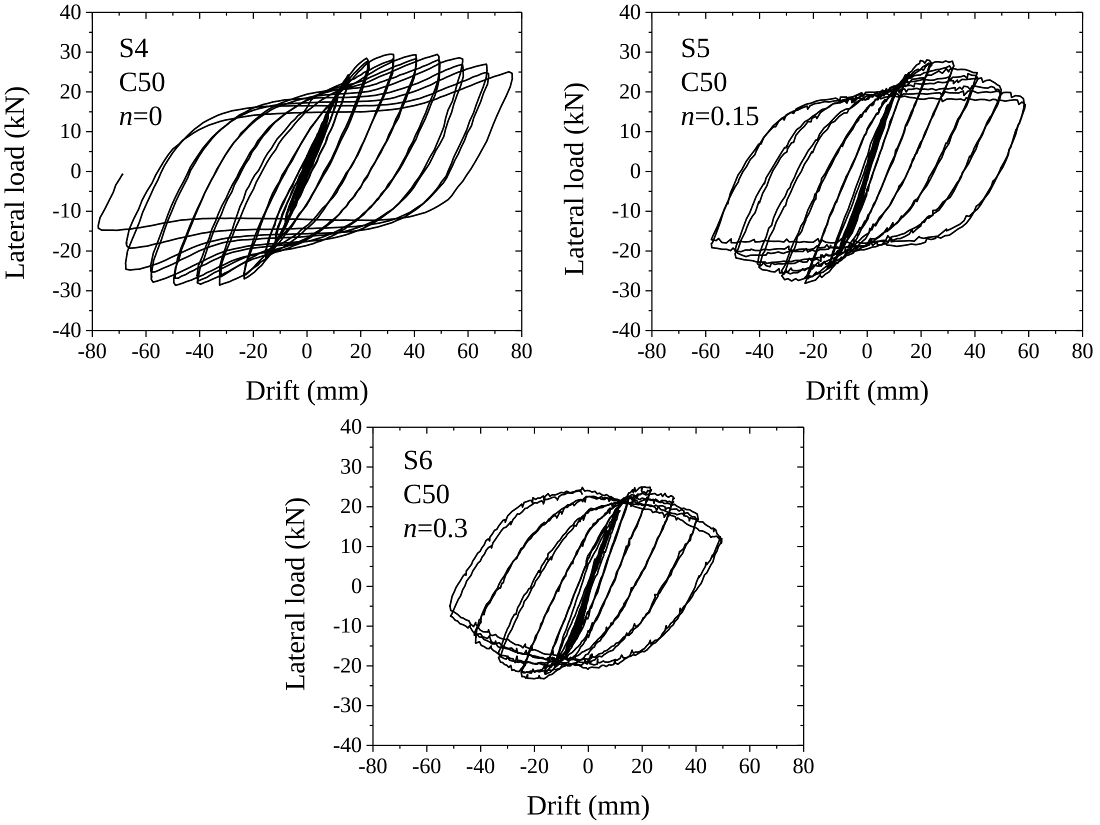

(b) Specimens filled with C50 concrete

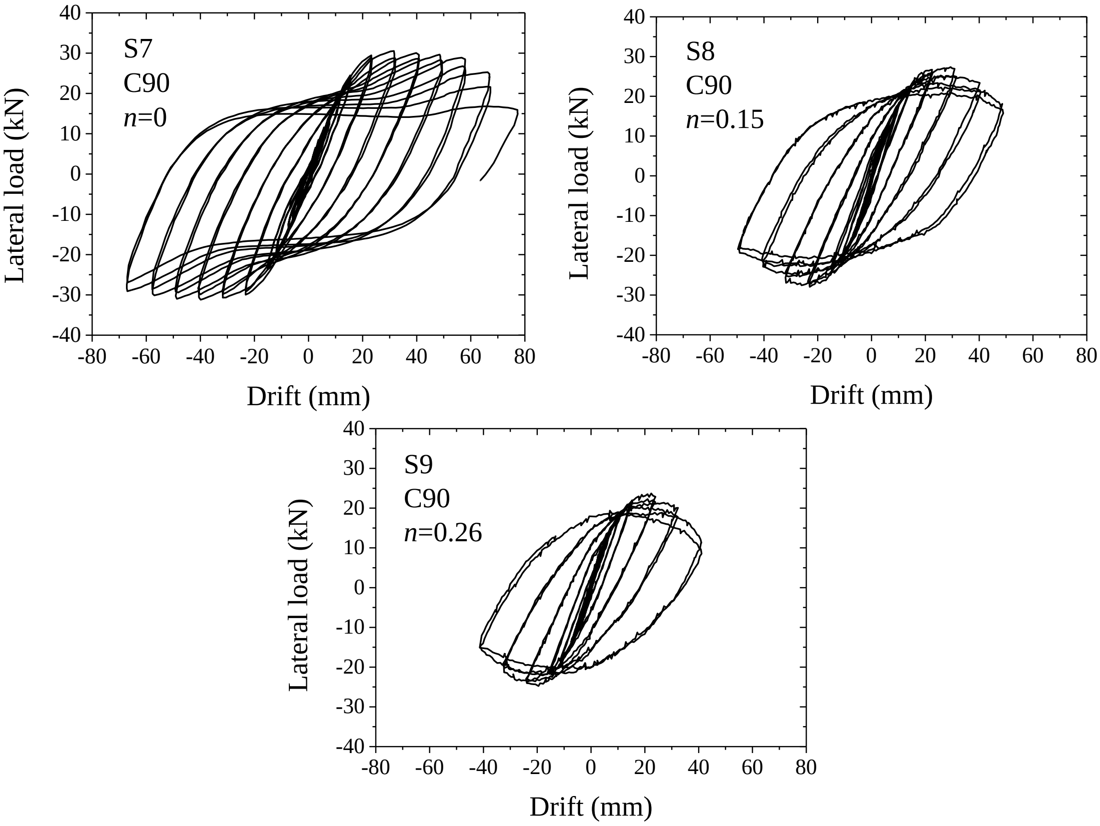

(c) Specimens filled with C90 concrete

Fig. 10. Lateral load and drift hysteretic curves.

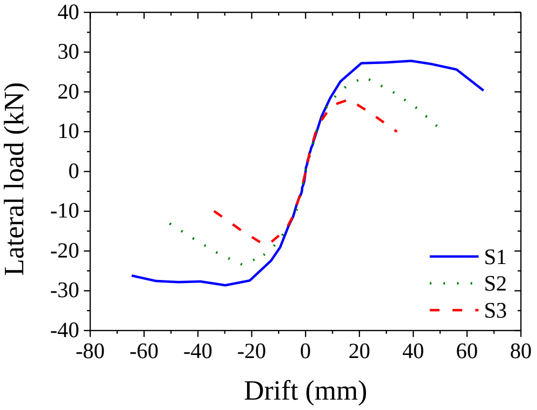

(a) Specimens filled with C30 concrete

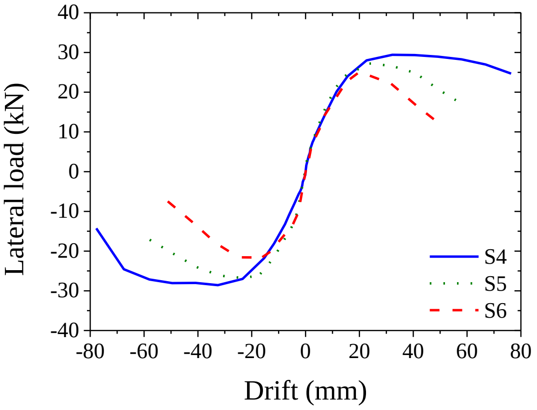

(b) Specimens filled with C50 concrete

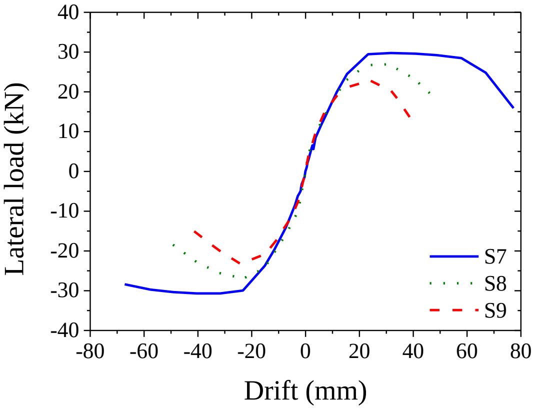

(c) Specimens filled with C90 concrete

Fig. 11. Lateral load and drift skeleton curves.

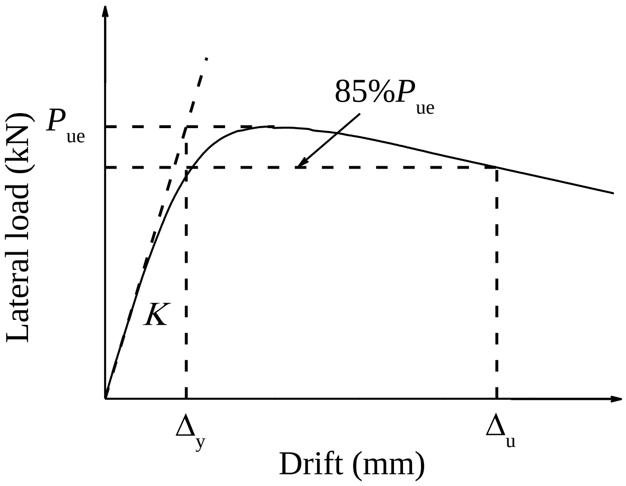

Fig. 12. Typical lateral load and drift curve.

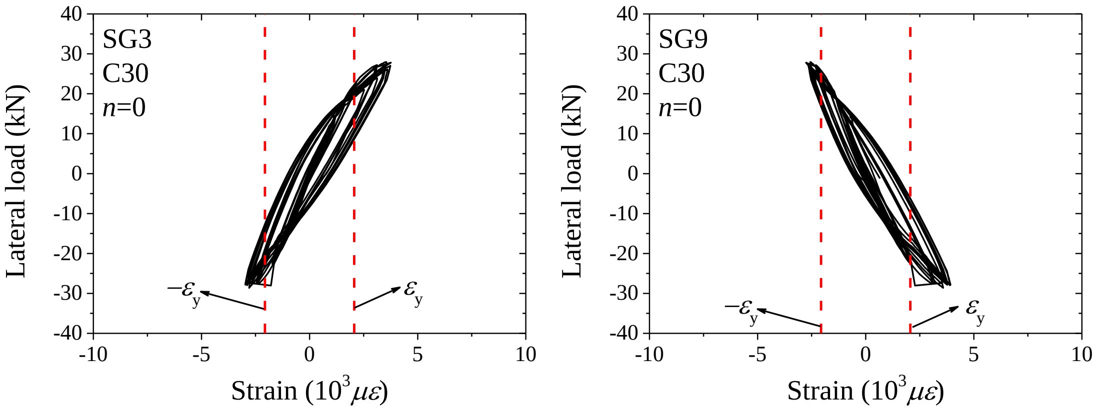

(a) B-B section

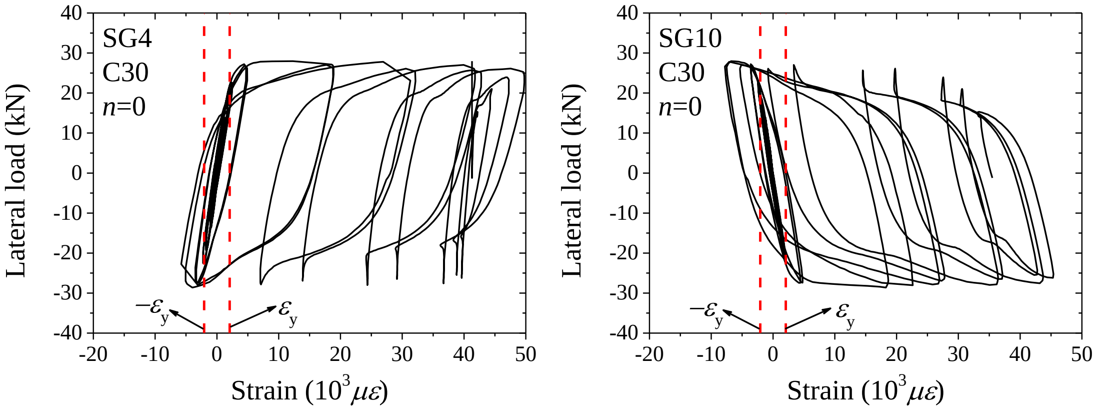

(b) A-A section

Fig 13. Lateral load versus steel strains in the S1 specimen (no axial load).

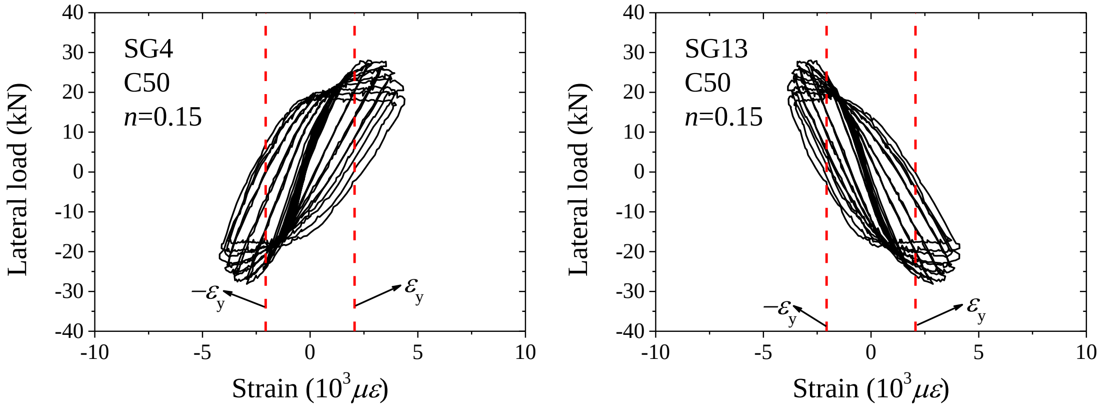

(a) B-B section

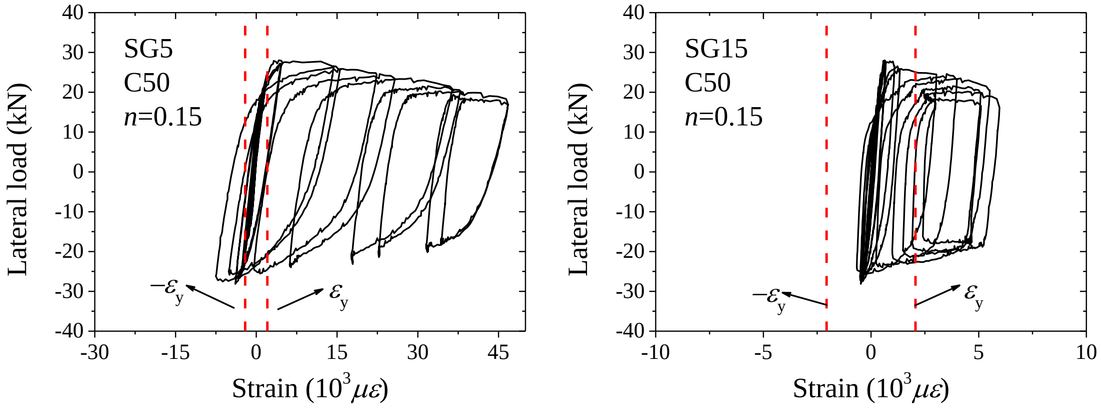

(b) A-A section (longitudinal strain)

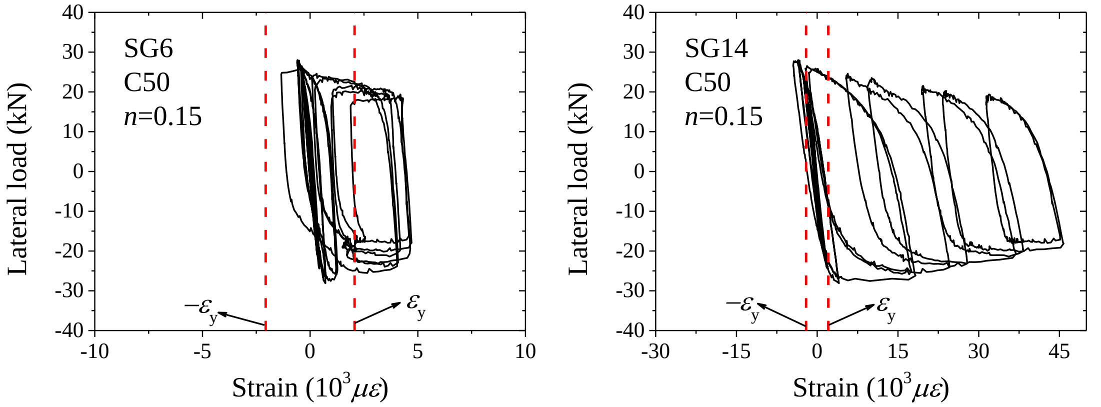

(c) A-A section (hoop strain)

Fig 14. Lateral load versus steel strains in the S5 specimen (moderate axial load).

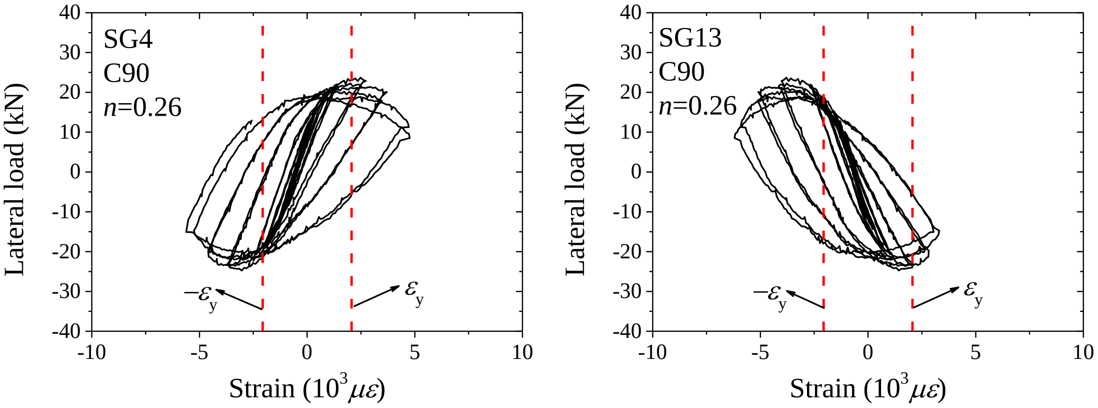

(a) B-B section

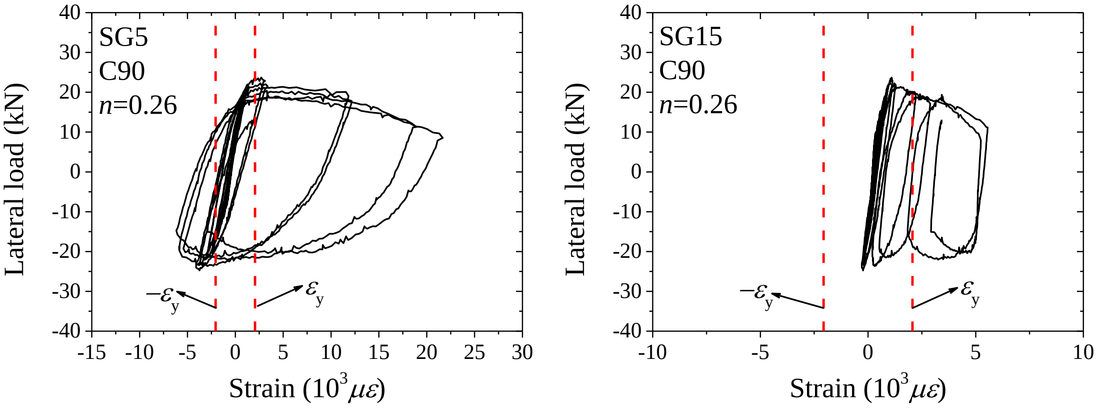

(b) A-A section (longitudinal strain)

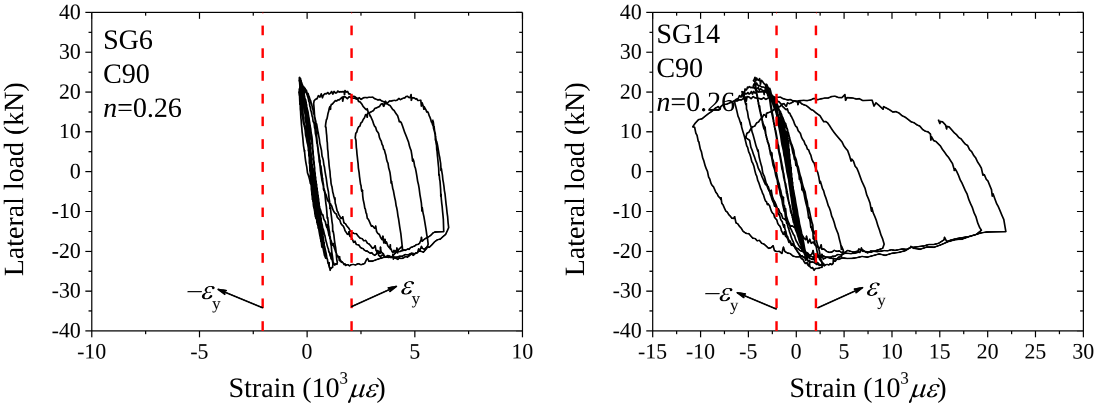

(c) A-A section (hoop strain)

Fig 15. Lateral load versus steel strains in the S9 specimen (high axial load).

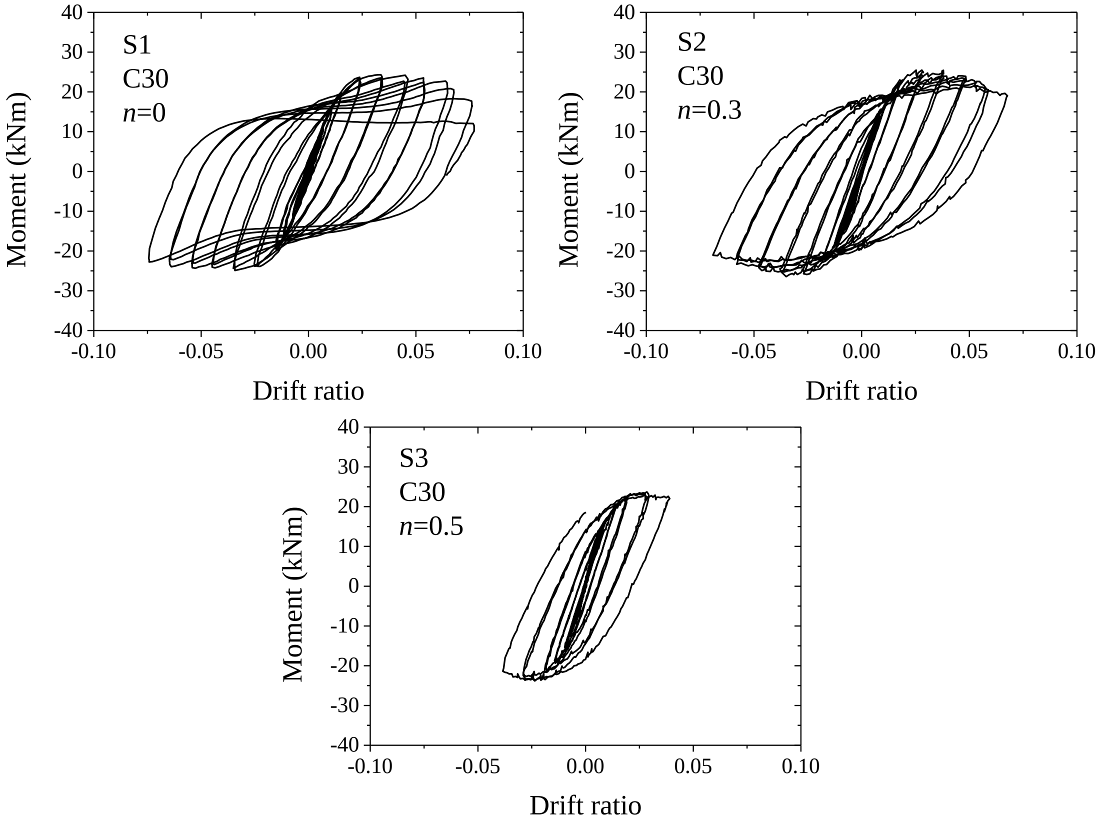

(a) Specimens filled with C30 concrete

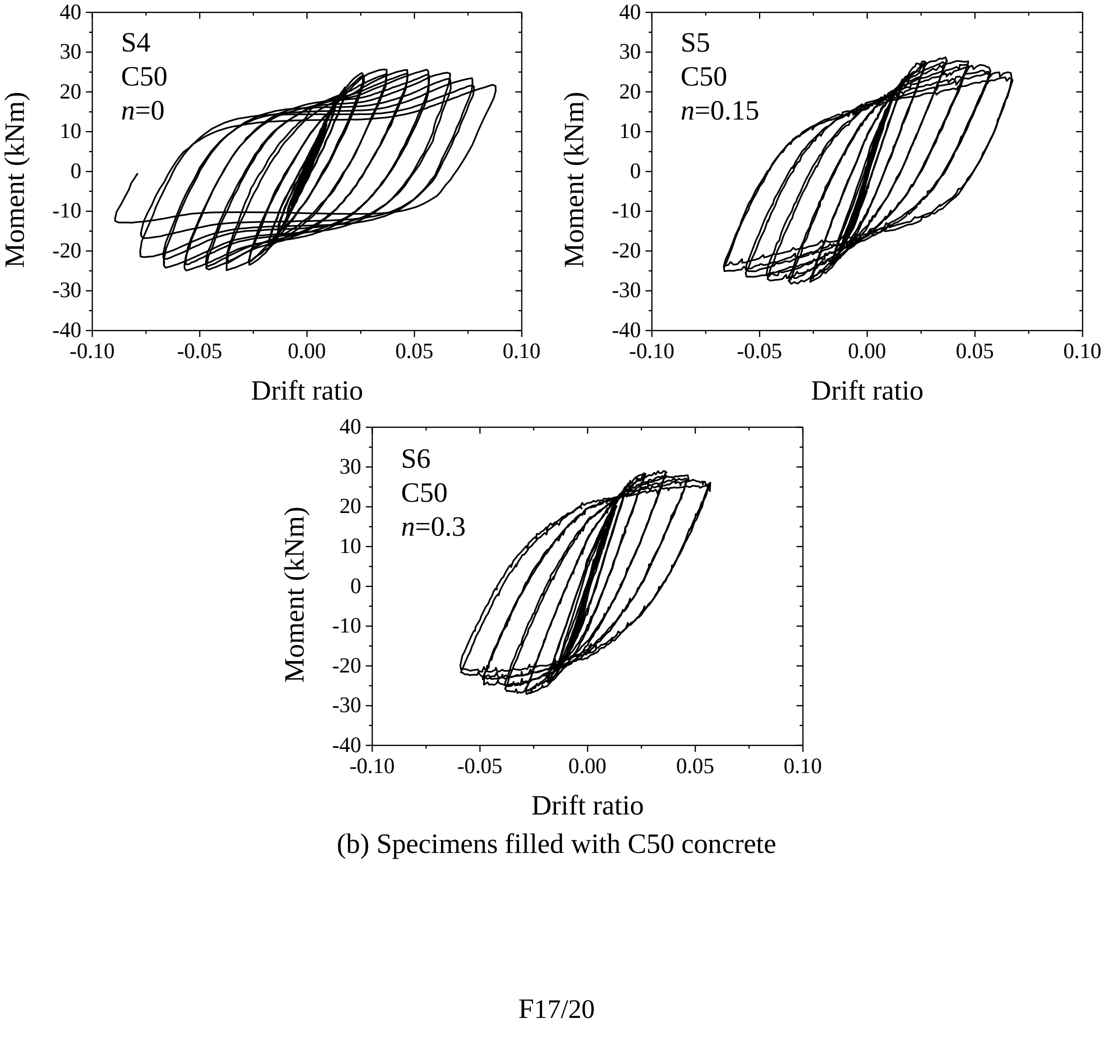

(b) Specimens filled with C50 concrete

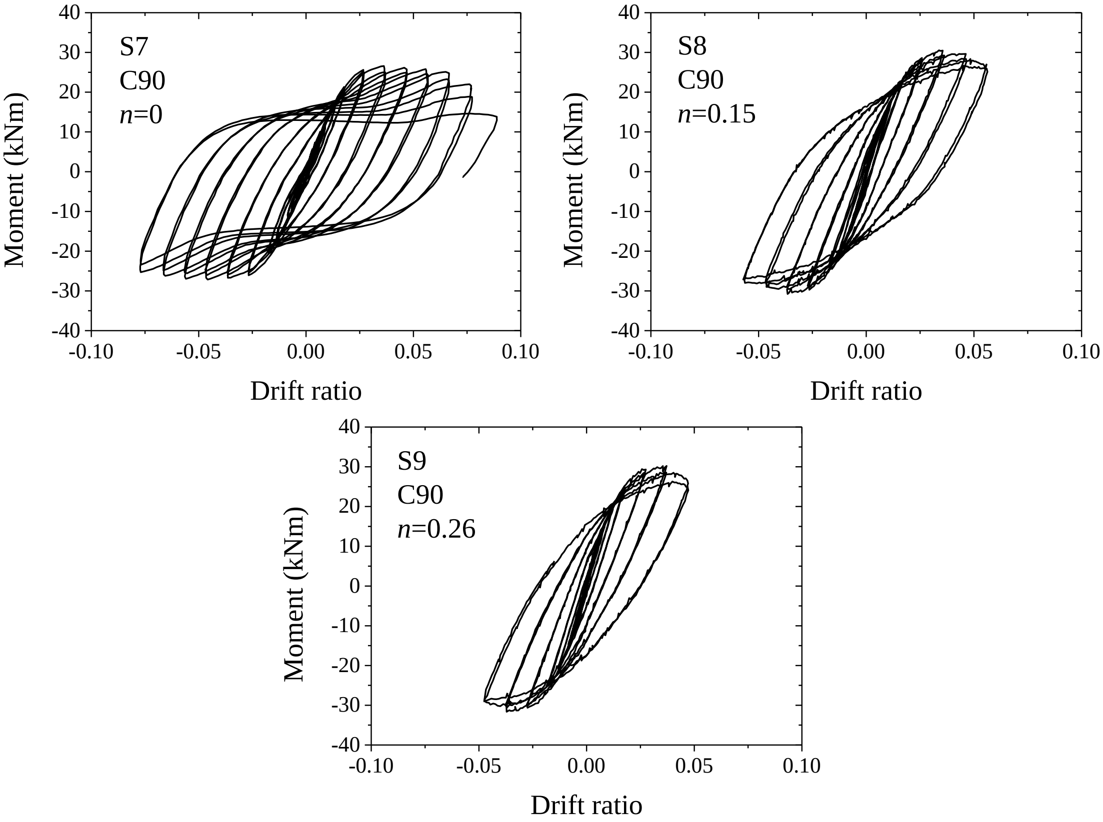

(c) Specimens filled with C90 concrete

Fig. 16. Moment and drift ratio hysteretic curves.

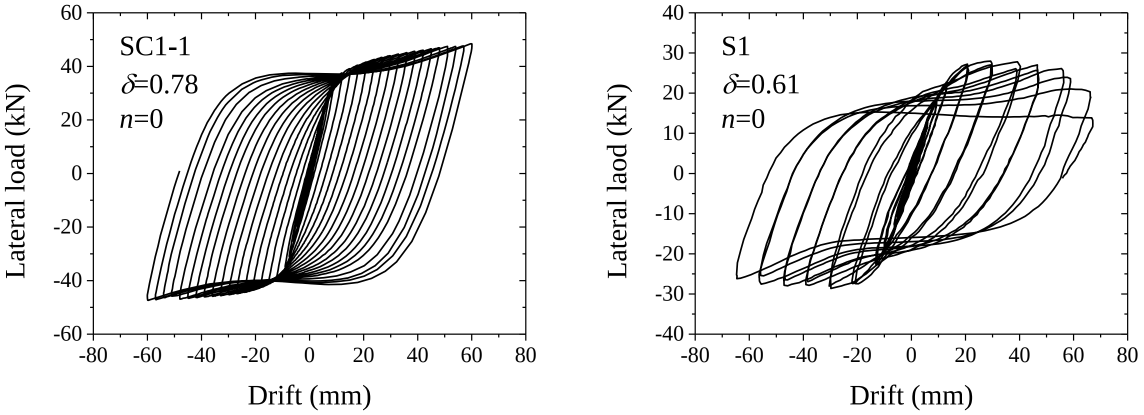

(a) Specimen SC1-1 in existing literature [2]

(b) Specimen S1

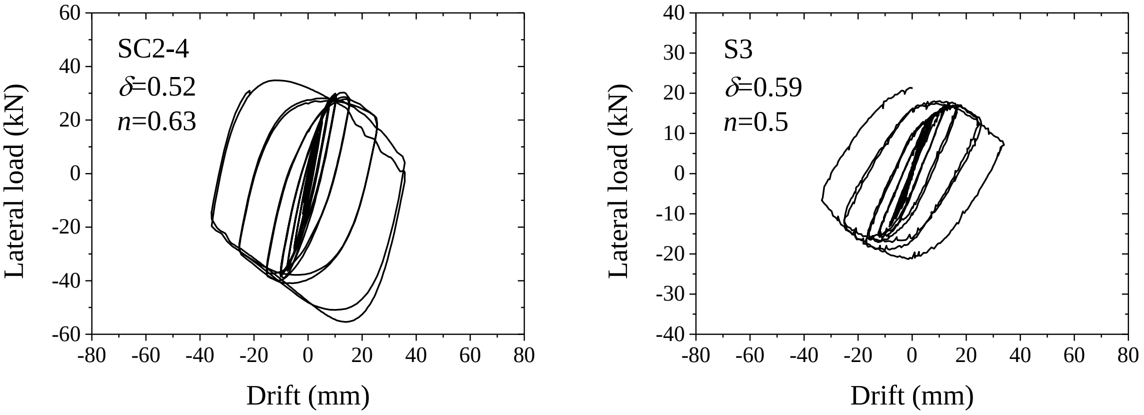

(c) Specimen SC2-4 in existing literature [2]

(d) Specimen S3

Fig. 17. Comparisons of lateral load vs drift curves of OCFST and CCFST beam-columns.

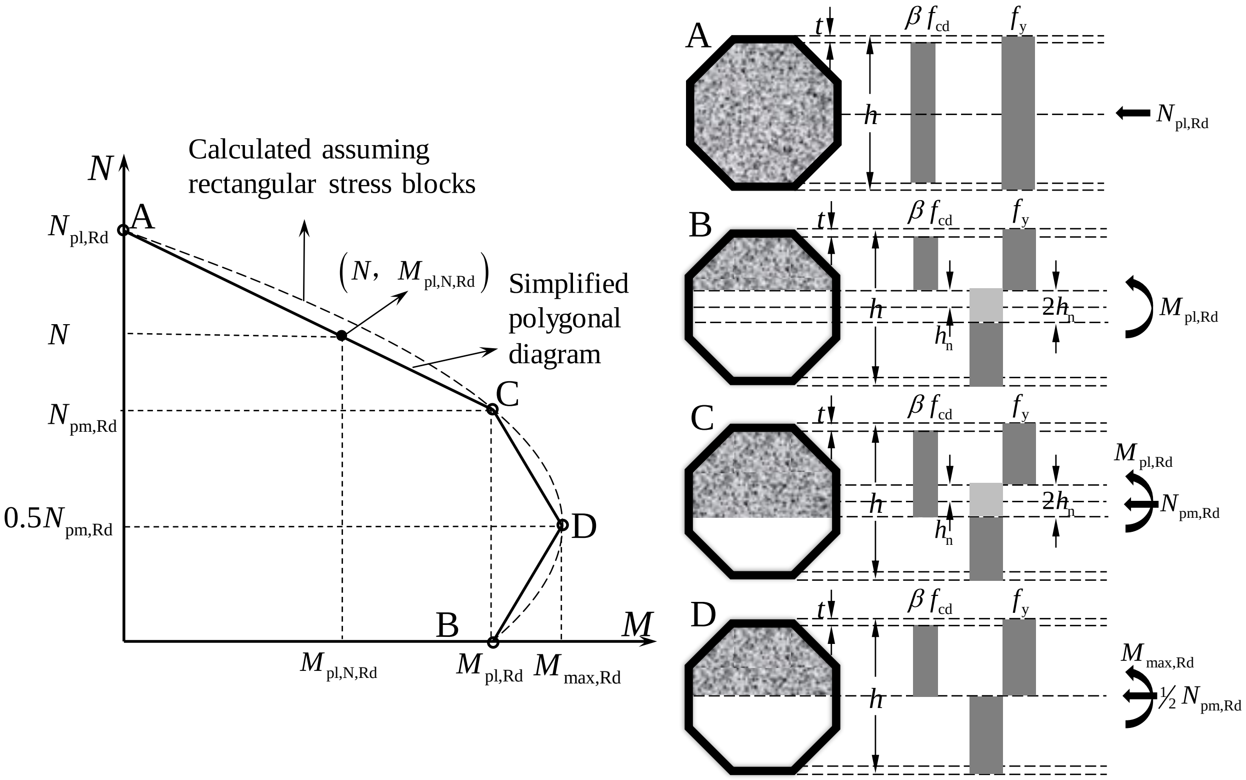

Fig. 18. Interaction curve and corresponding stress distributions according to EN 1994-1-1 [19].

Table 1

Detailed information of the test specimens.

Specimen	D (mm)	h (mm)	t (mm)	E_s (GPa)	f_y (MPa)	E_c (MPa)	$f_c^{'}$ (MPa)	δ -	D/t -	h/t -	N_u (kN)	Range of N_0 (kN)	Averaged N_0 (kN)	n -
S1	128.73	120.62	3.01	209.4	431.6	24538	30.0	0.61	42.8	40.1	781	-	0	0
S2	129.10	121.08	3.00	209.4	431.6	25054	32.1	0.59	43.0	40.4	806	230~250	240	0.3
S3	128.67	120.73	3.00	209.4	431.6	25007	32.3	0.59	42.9	40.2	804	380~420	400	0.5
S4	129.02	121.25	3.00	209.4	431.6	31532	50.5	0.48	43.0	40.4	1002	-	0	0
S5	128.87	120.89	3.00	209.4	431.6	31939	50.9	0.48	43.0	40.3	1007	140~160	150	0.15
S6	129.01	121.14	3.00	209.4	431.6	31702	51.7	0.47	43.0	40.4	1015	290~320	305	0.3
S7	129.13	120.96	3.00	209.4	431.6	41696	102.5	0.31	43.0	40.3	1558	-	0	0
S8	128.67	120.84	2.99	209.4	431.6	43799	104.6	0.31	43.0	40.4	1567	220~250	235	0.15
S9	128.31	120.57	3.00	209.4	431.6	42747	105.1	0.31	42.8	40.1	1569	380~420	400	0.26

Table 2
Cross-section slenderness limits.

Design provisions		Slenderness limits		Nominal yield strength		Measured yield strength	
		Circular D/t	Rectangular h/t	Circular D/t	Rectangular h/t	Circular D/t	Rectangular h/t
EN 1994-1-1		$90\times 235/f_{\mathrm{y}}$	$52\sqrt{235/f_{\mathrm{y}}}$	59.6	42.3	49.0	38.4
AISC 360-16 (compact)		$0.15E/f_{\mathrm{y}}$	$2.26\sqrt{E/f_{\mathrm{y}}}$	88.5	54.9	72.8	49.8
EN 1998-1	DCM ($q \leq 1.5$ - 2)	$90\times 235/f_{\mathrm{y}}$	$52\sqrt{235/f_{\mathrm{y}}}$	59.6	42.3	49.0	38.4
	DCM (1.5-2 < q < 4)	$85\times 235/f_{\mathrm{y}}$	$38\sqrt{235/f_{\mathrm{y}}}$	56.3	30.9	46.3	28.1
	DCH (q > 4)	$80\times 235/f_{\mathrm{y}}$	$24\sqrt{235/f_{\mathrm{y}}}$	53.0	19.5	43.6	17.7
AISC 341-16	λ_{hd}	$0.085E/R_{\mathrm{y}}f_{\mathrm{y}}$	$1.48\sqrt{E/R_{\mathrm{y}}f_{\mathrm{y}}}$	45.6	34.3	37.5	31.1
	λ_{md}	$0.17E/R_{\mathrm{y}}f_{\mathrm{y}}$	$2.37\sqrt{E/R_{\mathrm{y}}f_{\mathrm{y}}}$	91.2	54.9	75.0	49.8

Note:

R_{y} is taken as 1.1 for ASTM A572/A572M Gr. 50 (345) steel which is equivalent to European S355 steel.

Table 3
Test results of tensile coupon tests.

Coupon	E_s (GPa)	f_y (MPa)	ε_y ($\mu\varepsilon$)	ε_{st} -	f_u (MPa)	ε_u -	ε_f -
1	209.0	433.9	2076	0.0256	523.8	0.1708	0.3385
2	206.3	430.2	2085	0.0265	518.9	0.1740	0.3468
3	212.8	430.8	2024	0.0232	520.8	0.1711	0.3219
Average	*209.4*	*431.6*	*2062*	*0.0251*	*521.2*	*0.1720*	*0.3357*

Table 4
Concrete mix proportions and strengths.

Target cylinder strength (MPa)	Water/ cement	Water	Cement	Sand	Aggregate		S.P.[*1]	f_{c0}
					10mm	20mm		
	-	kg/m^3	kg/m^3	kg/m^3	kg/m^3	kg/m^3	kg/m^3	MPa
30	0.65	221	340	700	380	760	-	34.4
50	0.45	180	400	691	378	752	1.5	55.7
90	0.25	128	512	717	430	645	10	105.8

Note: *[1]. S.P. is superplasticizer.

Table 5
Summary of the test results and comparison with code provisions.

Specimen		Experimental results					EN 1994-1-1				AISC 360-16			
	P_{ue}	M_{ue}	K_{ie}	E_h	$E_{h,4\%}$	μ	M_{uc}	M_{ue}/M_{uc}	K_{ic}	K_{ie}/K_i	M_{uc}	M_{ue}/M_{uc}	K_{ic}	K_{ie}/K_i
	(kN)	(kNm)	(kNm·m)	(kNm)	(kNm)	-	(kNm)	-	(kNm·m)	-	(kNm)	-	(kNm·m)	-
S1	28.29	24.61	836	24.47	4.62	6.36	22.40	1.099	1122	0.745	22.23	1.107	1184	0.706
S2	23.82	25.97	1287	18.66	4.74	4.76	23.70	1.096	1128	1.141	23.49	1.106	1191	1.081
S3	21.36	23.76	1356	5.01	-	3.23	19.02	1.249	1127	1.203	18.87	1.259	1191	1.139
Mean								*1.148*		*1.030*		*1.157*		*0.975*
COV								*0.076*		*0.241*		*0.076*		*0.241*
S4	29.05	25.27	872	30.74	4.73	6.65	23.04	1.097	1198	0.728	22.80	1.108	1278	0.682
S5	28.07	28.48	1401	20.53	4.95	4.74	25.57	1.114	1203	1.165	25.26	1.127	1284	1.091
S6	24.12	28.07	1648	15.58	5.17	4.32	26.96	1.041	1200	1.373	26.49	1.060	1281	1.286
Mean								*1.084*		*1.089*		*1.098*		*1.020*
COV								*0.035*		*0.303*		*0.032*		*0.302*
S7	30.87	26.86	905	28.43	4.62	5.66	24.44	1.099	1309	0.691	24.04	1.117	1414	0.640
S8	27.64	30.66	1672	13.47	5.17	4.58	29.07	1.055	1332	1.255	28.40	1.080	1443	1.159
S9	24.23	30.92	2183	8.81	4.57	4.19	31.94	0.968	1320	1.654	31.13	0.993	1429	1.528
Mean								*1.041*		*1.200*		*1.063*		*1.109*
COV								*0.064*		*0.403*		*0.060*		*0.402*
Overall Mean								**1.091**		**1.106**		**1.106**		**1.034**
Overall COV								**0.068**		**0.295**		**0.064**		**0.291**

Table 6

Contribution of second-order effects (case 1).

Specimen	Experimental results				
	M_{ue} (kNm)	*1st order moment due to PL_f* (kNm)	*Contribution due to 1st order moment (%)* -	*2nd order moment due to $N_{ver}\Delta$* (kNm)	*Contribution due to 2nd order moment (%)* -
S2	25.97	20.01	77.1	5.96	22.9
S3	23.76	14.05	59.1	9.71	40.9
S5	28.48	24.08	84.6	4.40	15.4
S6	28.07	19.73	70.3	8.34	29.7
S8	30.66	23.72	77.4	6.94	22.6
S9	30.92	17.36	56.1	13.56	43.9

Table 7
Contribution of second-order effects (case 2).

Specimen	Experimental results				
	M_u' (kNm)	*1st order moment due to PL_f* (kNm)	*Contribution due to 1st order moment (%)* -	*2nd order moment due to $N_{ver}\Delta$* (kNm)	*Contribution due to 2nd order moment (%)* -
S2	19.02	5.42	28.5	12.78	67.2
S3	22.02	8.67	39.4	13.34	60.6
S5	23.05	14.61	63.4	8.44	36.6
S6	26.10	10.47	40.1	15.63	59.9
S8	25.12	13.67	54.4	11.45	45.6
S9	24.07	7.42	30.8	16.64	69.2

Table 8

Summary of the selected tests [2].

Specimen	D	t	L	f_y	f_{cu}	f_c'	δ	n
	mm	mm	mm	MPa	MPa	MPa	-	-
SC1-1	108	4.00	855	356.0	22.0	16.9	0.78	0.00
SC2-4	114	3.00	855	308.0	38.9	31.9	0.52	0.63